Int. J. Fuzzy Syst.
https://doi.org/10.1007/s40815-025-02149-z

A New Fuzzy Clustering Algorithm for Image Segmentation

Ali Fahmi Jafargholkhanloo[1] · **Mousa Shamsi**[2] · **Mahdi Bashiri Bawil**[2] · **Sebelan Danishvar**[3]

Received: 9 March 2025 / Revised: 9 June 2025 / Accepted: 31 August 2025

Abstract The fuzzy c-means (FCM) algorithm is widely used image segmentation but, has several limitations. It is sensitive to noise, demonstrates variable convergence rate depending on data distribution, and its reliance on Euclidean distance fails to account for intra-cluster variations, particularly in complex and color images. Furthermore, FCM's non-adaptive distance metric struggles with diverse cluster shapes, and most FCM-based approaches face difficulties in color image segmentation due to the challenges in spatial information acquisition. To address these limitations, we propose an Improved Gustafson-Kessel (IGK) algorithm that offers superior robustness compared to both FCM and traditional Gustafson-Kessel (GK) clustering. Our approach first applies morphological reconstruction (MR) for grayscale images and multivariate morphological reconstruction (MMR) for color images to ensure noise immunity while preservation image details. We then replace the Euclidean distance metric with Mahalanobis distance to adapt to varying cluster shapes. The algorithm iteratively updates cluster centers, membership matrix, and positive definite symmetric matrices, followed by a median filter refinement of the membership partition matrix. Unlike previous approaches, IGK eliminates the need for computing distances within local spatial neighbors during clustering. Experimental results on both grayscale and color images demonstrate that the proposed IGK algorithm achieves superior segmentation performance compared to existing FCM-based methods.

Keywords Fuzzy c-means (FCM) clustering · Gustafson-Kessel (GK) clustering · Image segmentation · Mahalanobis distance · Morphological reconstruction (MR)

✉ Sebelan Danishvar
sebelan.danishvar@brunel.ac.uk

Ali Fahmi Jafargholkhanloo
a_fahmi@uma.ac.ir

Mousa Shamsi
shamsi@sut.ac.ir

Mahdi Bashiri Bawil
m_bashiri99@sut.ac.ir

[1] Department of Engineering Sciences, Faculty of Advanced Technologies, University of Mohaghegh Ardabili, Namin, Iran

[2] Faculty of Biomedical Engineering, Sahand University of Technology, Tabriz, Iran

[3] College of Engineering, Design and Physical Sciences, Brunel University London, Uxbridge UB8 3PH, UK

1 Introduction

Image segmentation divides an image into meaningful regions based on features such as grayscale values, color, spatial texture, and geometry [1,2]. This fundamental process in image processing and computer vision can be categorized into four primary approaches: threshold-based methods [3,4], which classify pixels by setting single or multiple grayscale thresholds; contour-based methods [5,6], which use energy functions for segmentation; training-based methods [7,8], which apply supervised learning for segmentation; and clustering-based methods [9,10]. Among these, clustering approaches have gained particular prominence due to their ability to group data into clusters where intra-cluster similarity is minimized. Fuzzy c-means (FCM)-based techniques, which focus on cost function minimization, have become especially popular within the clustering domain. This paper focuses on these enhancing FCM-based methods.

Szilágyi et al. [11] proposed an enhanced FCM (EnFCM) algorithm that uses grayscale histograms for MRI brain image segmentation, achieving significant reduction in pro-

Published online: 17 November 2025

cessing time. Cai et al. [12] introduced a fast generalized FCM (FGFCM) algorithm to address EnFCM's limitations by incorporating a new local similarity index parameter, ζ_{ij}, which enhances noise robustness while preserving image details. Krinidis and Chatzis [13] presented fuzzy local information c-means (FLICM), which employs a novel fuzzy factor, G_{ki}, as a local similarity index to replace EnFCM's α parameter. However, FLICM's fixed spatial distance limits its adaptability to varying local image information. To overcome this limitation, Gong et al. [14] developed KWFLICM, introducing a weighted fuzzy factor that balances image detail and noise without requiring empirically tuned parameters. Despotović et al. [15] suggested spatially coherent FCM (SCFCM) to improve noise robustness by integrating neighboring pixel information via phase congruency, anisotropic neighborhoods, and adaptive weights.

Xiang et al. [16] proposed kernel-based FCM with intensity and location information (ILKFCM) for SAR image segmentation, involving wavelet decomposition, fuzzy factor computation, and iteration. Elazab et al. [17] introduced adaptively regularized kernel-based FCM (ARKFCM) for MRI segmentation, using Gaussian radial basis kernels in place of Euclidean distance to handle grayscale inhomogeneity, though it struggles with unknown noise. Bakhshali [18] introduced a robust FCM using information theory to reduce MRI noise and correct bias fields. Chaomurilige et al. [19] applied deterministic annealing to the Gustafson-Kessel (GK) algorithm, minimizing the influence of clustering parameters by incorporating Shannon's entropy. Bai et al. [20] presented intuitionistic center-free FCM (ICF-FCM) for MRI segmentation, which uses pixel-to-pixel and pixel-to-cluster similarities for noise reduction and vagueness handling, while Bai et al. [21] proposed possibilistic FCM (PFCM) for MRI segmentation, leveraging intraclass and interclass similarities to manage outliers and enhance detail preservation.

Lei et al. [9] developed a fast and robust FCM (FRFCM), integrating morphological reconstruction (MR) for preprocessing and membership filtering for post-processing. While effective for grayscale images, its performance on complex images is sometimes limited. Hu et al. [22] suggested intuitionistic kernel-based FCM (IFCM) for power equipment segmentation, which, though effective, is computationally intensive. Kumar et al. [23] developed a bias-corrected FCM with spatial neighborhood information (BCIF CMSNI) to handle MRI noise and bias fields, employing Sugeno's and Yager's negation functions to convert images into intuitionistic fuzzy sets (IFS). Zhang et al. [24] introduced total generalized variation FCM (TGVFCM), incorporating a regularization term to enhance quality. Wang et al. [25] employed sparse regularization with MR and wavelet frames in SRFCM for robust clustering. Finally, Wang et al. [26] presented residual-driven FCM (RFCM), incorporating weighted ℓ_2-norm regularization to improve noise handling.

Based upon these prior studies, we propose a significantly improved GK algorithm (IGK) for image segmentation that achieves high accuracy across diverse image types. Our main contributions are:

(1) **Geometric Adaptability**: Unlike FRFCM [9] and other FCM-based algorithms [10–17,26], that employ spherical clusters, IGK supports elliptical cluster shapes, enhancing segmentation accuracy across different image types.
(2) **Noise Robustness**: The proposed IGK applies Morphological Reconstruction (MR) [27,28] to preserve detail and mitigate noise in both grayscale and color images, achieving higher robustness than other FCM-based methods. A simplified histogram calculation method also enables fast segmentation.
(3) **Enhanced Distance Metric**: IGK replaces Euclidean distance with Mahalanobis distance to adapt to cluster shapes, improving segmentation performance, particularly in color images.

The remainder of this paper is organized as follows: Section 2 reviews related work in fuzzy clustering. Section 3 describes the proposed methodology. Section 4 presents experimental results with grayscale image segmentation discussed in Section 4.3 and color image segmentation in Section 4.5. Finally, Section 5 provides conclusions and directions for future research.

2 Related Works

The proposed algorithm's performance will be compared with several established clustering algorithms, including FCM, GK, EnFCM, FGFCM, FLICM, ARKFCM, KWFLICM, FRFCM, and RFCM. This section provides an overview of each algorithm.

2.1 FCM

The FCM algorithm, introduced by Bezdek [29], enhances the K-means algorithm using a membership matrix u_{ij}. The cost function in FCM is defined as:

$$J_{FCM} = \sum_{i=1}^{N} \sum_{j=1}^{c} {u_{ij}}^{q} \left(x_i - v_j\right)^2 \tag{1}$$

where v_j and q represent the cluster center and fuzzy exponent, respectively. In FCM, the membership function and

cluster centers are iteratively updated as follows:

$$u_{ij} = \frac{1}{\sum_{j=1}^{c} \left(\frac{\|x_i - v_k\|^2}{\|x_i - v_j\|^2} \right)^{\frac{2}{q-1}}} \tag{2}$$

$$v_j = \frac{\sum_{i=1}^{N} \left({u_{ij}}^q x_i \right)}{\sum_{i=1}^{N} \left({u_{ij}}^q \right)} \tag{3}$$

The membership matrix u_{ij} quantifies the extent to which the data point x_i is associated with cluster j, based on its relative distances to all cluster centers. As shown in Eq. (3), the cluster centers are computed as weighted averages of the data points, where the weights correspond to the membership degrees raised to the power q.

2.2 GK

While FCM assumes clusters spherical, making it suitable for data with uniformly sized and shaped clusters, the GK algorithm extends FCM to detect ellipsoidal clusters of varying sizes and orientations [30,31]. GK adapts distance calculations to cluster shapes by estimating the covariance matrix [32]. Gustafson and Kessel [33] modified FCM using the Mahalanobis distance for diverse geometrical shapes. The GK cost function is:

$$J_{GK} = \sum_{i=1}^{N} \sum_{j=1}^{c} {u_{ij}}^q . \left(x_i - v_j \right)^T . A_j . \left(x_i - v_j \right) \tag{4}$$

where A_j is a positive definite symmetric matrix. Using the Lagrange multiplier technique, the equation (4) can be converted to an unconstrained optimization problem that minimizes the following cost function:

$$\begin{aligned} J_{GK} = & \sum_{i=1}^{N} \sum_{j=1}^{c} {u_{ij}}^q . \left(x_i - v_j \right)^T . A_j . \left(x_i - v_j \right) \\ & - \sum_{i=1}^{N} \lambda_i \left(\sum_{j=1}^{c} u_{ij} - 1 \right) \\ & + \sum_{j=1}^{c} \beta_j . \left(det \left(A_j \right) - \rho_j \right) \end{aligned} \tag{5}$$

where β_j is a set of Lagrange multipliers, and ρ_j, typically set to 1, represents cluster volume. The membership function, cluster centers, and covariance matrix are updated as follows [33]:

$$u_{ij} = \left(\frac{\left(x_i - v_r \right)^T . A_r . \left(x_i - v_r \right)}{\sum_{j=1}^{c} \left(x_i - v_j \right)^T . A_j . \left(x_i - v_j \right)} \right)^{1/q-1} \tag{6}$$

$$v_j = \frac{\sum_{i=1}^{k} {u_{ij}}^q . x_i}{\sum_{i=1}^{k} {u_{ij}}^q} \tag{7}$$

$$F_i = \frac{\sum_{i=1}^{N} {u_{ij}}^q . \left(x_i - v_j \right)^T . \left(x_i - v_j \right)}{\sum_{i=1}^{N} {u_{ij}}^q} \tag{8}$$

$$A_j = \lambda_i . \left(det \left(F_i \right) \right)^{\frac{1}{n}} . F_i^{-1} \tag{9}$$

Equation (6) defines the updated membership matrix, which incorporates an adaptive distance metric specific to each cluster. The cluster centers are updated in Eq. (7) as the weighted mean of the data points, following a procedure similar to that of the Fuzzy C-Means (FCM) algorithm. The fuzzy covariance matrix, given in Eq. (8), characterizes the spread and orientation of data within each cluster. Furthermore, Eq. (9) defines the matrix A_j, which adjusts the shape of each cluster using the inverse of its covariance matrix, scaled appropriately to satisfy the determinant constraint.

2.3 EnFCM

The EnFCM algorithm, an FCM improvement, speeds up MRI brain image segmentation by working on the gray-level histogram of a reconstructed image ξ_i (a weighted sum image based on original image and its local neighbor average) [11]. Its objective function is:

$$J_{EnFCM} = \sum_{i=1}^{N} \sum_{j=1}^{c} \gamma_i {u_{ij}}^q \left(\xi_i - v_j \right)^2 \tag{10}$$

where γ_i denotes the number of pixels with a gray value i, $(i = 1, 2, \ldots, k)$. Generally, we have:

$$\sum_{i=1}^{N} \gamma_i = 1 \tag{11}$$

$$\xi_r = \frac{1}{1+\alpha} \left(x_r + \frac{\alpha}{N_L} \sum_{j \in N_r} x_j \right) \tag{12}$$

where N_L represents the number of pixels in a window around x_r. The membership function and cluster centers are updated as:

$$u_{ij} = \left[\sum_{j=1}^{c} \left(\frac{\xi_i - v_k}{\xi_i - v_j} \right)^{\frac{2}{q-1}} \right]^{-1} \tag{13}$$

$$v_j = \frac{\sum_{i=1}^{N} \left(\gamma_i {u_{ij}}^q \xi_i \right)}{\sum_{i=1}^{N} \left(\gamma_i {u_{ij}}^q \right)} \tag{14}$$

In the EnFCM algorithm, the membership matrix is updated based on the distances between the reconstructed intensities and the cluster centers. The cluster centers are then updated as the weighted average of gray levels ξ_i, incorporating both the membership values and the corresponding frequency weights.

2.4 FGFCM

FGFCM combines local spatial and gray information to enhance EnFCM by overcoming noise sensitivity using a

local similarity index ζ_{ij} and removing the empirically-adjusted parameter α in image segmentation process. This algorithm improves the performance of EnFCM algorithm. ζ_{ij} function is defined as follows [12]:

$$\xi_{ij} = \begin{cases} \xi_{s\_ij} \times \xi_{g\_ij}, \ i \neq j \\ 0, \ i = j \end{cases} \tag{15}$$

where ξ_{s_ij} and ξ_{g_ij} represent local spatial and local gray-level relationships, respectively. These functions can be defined as [12]:

$$\xi_{s\_ij} = \exp\left(\frac{-\max\left(\left|L_i - L_j\right|, \left|K_i - K_j\right|\right)}{\lambda_s}\right) \tag{16}$$

$$\xi_{g\_ij} = \exp\left(\frac{-\left\|x_i - x_j\right\|^2}{\lambda_g \times \sigma_{g\_i}^2}\right) \tag{17}$$

$$\sigma_{g\_i} = \sqrt{\frac{\sum_{j\epsilon \ i}\left\|x_i - x_j\right\|^2}{N_L}} \tag{18}$$

where (L_i, K_i) is a spatial coordinate of the ith pixel. λ_s represents the scale factor of the spread of ξ_{s_ij}. λ_g is the global scale factor of the spread of ξ_{g_ij}. σ_{g_i} denotes the local density surrounding the central pixel.

2.5 FLICM

Krinidis and Chatzis [13] introduced the FLICM algorithm, which uses a fuzzy factor G_{ki} that incorporates local spatial and gray-level information without empirical parameter adjustments, and overcomes the noise problems in image segmentation. In this algorithm, G_{ki} is introduced based on Eq. (19) [13]:

$$G_{ki} = \sum\nolimits_{j\in N_i} \frac{1}{l_{ij}+1}\left(1-u_{kj}\right)^q . \left\|x_j - v_k\right\|^2, \ i \neq j \tag{19}$$

where l_{ij} is the spatial Euclidean distance between pixels i and j. The cost function in FLICM is defined as [13]:

$$J_{FLICM} = \sum\nolimits_{i=1}^{N}\sum\nolimits_{j=1}^{c}\left({u_{ij}}^q . \left\|x_i - v_j\right\|^2 + G_{ij}\right) \tag{20}$$

The membership function and cluster centers are updated as [13]:

$$u_{ij} = \frac{1}{\sum_{j=1}^{c}\left(\frac{\left\|x_i - v_k\right\|^2 + G_{kj}}{\left\|x_i - v_j\right\|^2 + G_{ij}}\right)^{\frac{1}{m-1}}} \tag{21}$$

$$v_j = \frac{\sum_{i=1}^{N}\left({u_{ij}}^q x_i\right)}{\sum_{i=1}^{N}\left({u_{ij}}^q\right)} \tag{22}$$

Equation (21) defines the updated membership function, in which the effect of each cluster is modulated not only by the feature-space distance but also by the local spatial information through the term G_{ij}. Similarly, Eq. (22) specifies the update rule for the cluster centers, which are computed as the weighted average of the data points, following the conventional approach used in FCM.

2.6 ARKFCM

ARKFCM enhances FCM with an adaptive regularization term that controls pixel neighbor effects based on local grayscale distribution. It applies a kernel function instead of Euclidean distance. The cost function is defined as [17]:

$$J_{ARKFCM} = 2\left[\sum\nolimits_{i=1}^{N}\sum\nolimits_{j=1}^{c}{u_{ij}}^q . \left(1 - K\left(x_i, \ v_j\right)\right) + \varphi_i . {u_{ij}}^q \right. \\ \left. . \left(1 - K\left(\bar{x}_i, \ v_j\right)\right)\right] \tag{23}$$

where φ_i denotes the assigned weight to every pixel and $\bar{x}_i$ is mean grayscale of image pixels. $K\left(x_i, \ v_j\right)$ is a Gaussian Radial-based Function (GRBF) and defined as follows with a kernel width (σ) [17]:

$$K\left(x_i, \ v_j\right) = \exp\left(-\frac{\left\|x_i - v_j\right\|^2}{2\sigma^2}\right) \tag{24}$$

The membership function and cluster centers are updated by [17]:

$$u_{ij} = \frac{\left(1 - K\left(x_i, \ v_k\right) + \varphi_i\left(1 - K\left(\bar{x}_i, \ v_k\right)\right)\right)^{-1/(q-1)}}{\sum_{j=1}^{c}\left(1 - K\left(x_i, \ v_j\right) + \varphi_i\left(1 - K\left(\bar{x}_i, \ v_j\right)\right)\right)^{-1/(q-1)}} \tag{25}$$

$$v_j = \frac{\sum_{i=1}^{N}{u_{ij}}^q . \left(K\left(x_i, v_j\right) x_i + \varphi_i . K\left(\bar{x}_i, \ v_j\right)\bar{x}_i\right)}{\sum_{i=1}^{N}{u_{ij}}^q . \left(K\left(x_i, v_j\right) x_i + \varphi_i . K\left(\bar{x}_i, \ v_j\right)\right)} \tag{26}$$

As defined in Eq. (25), both the original intensity and the local average intensity contribute to the membership assignment, thereby introducing spatial regularization without the need for explicit empirical parameters. The cluster centers, updated according to Eq. (26), are computed as a weighted average that integrates both the original and spatially regularized terms, with the weights modulated by the corresponding kernel values.

2.7 KWFLICM

The KWFLICM algorithm introduces a kernel-based approach using a trade-off weighted fuzzy factor $\acute{G}_{ij}$ to improve FLICM. This approach depends on the space distance of all neighboring pixels and their gray-level difference simultaneously. The presented weighted fuzzy factor can accurately estimate the damping extent of neighboring pixels. Also,

a kernel distance is added to objective function, making it robust to noise and outliers. The objective function is [14]:

$$J_{KWFLICM} = \sum_{i=1}^{N} \sum_{j=1}^{c} u_{ij}{}^{q} . \left(1 - K\left(x_i, v_j\right)\right) + \acute{G}_{ij} \tag{27}$$

where $\acute{G}_{ij}$ is defined as [14]:

$$\acute{G}_{ij} = \sum_{i=1}^{N} \sum_{j=1}^{c} u_{ij}{}^{q} . \sum_{k \in N_i} w_{ik} \left(1 - u_{ij}\right)^{q} . \left(1 - K\left(x_k, v_j\right)\right), \; i \neq k \tag{28}$$

The membership function and cluster centers are updated by [14]:

$$u_{ij} = \left(\frac{\left(1 - K\left(x_i, v_l\right)\right) + \sum_{k \in N_i} w_{ik} \left(1 - u_{ij}\right)^{q} . \left(1 - K\left(x_k, v_l\right)\right), \; i \neq k}{\sum_{j=1}^{c} \left(1 - K\left(x_i, v_j\right)\right) + \sum_{k \in N_i} w_{ik} \left(1 - u_{ij}\right)^{q} . \left(1 - K\left(x_k, v_j\right)\right), \; i \neq k} \right)^{1/(q-1)} \tag{29}$$

$$v_j = \frac{\sum_{i=1}^{N} \left(u_{ij}{}^{q} . K\left(x_i, v_j\right) . x_i\right)}{\sum_{i=1}^{N} \left(u_{ij}{}^{q} . K\left(x_i, v_j\right)\right)} \tag{30}$$

Also, w_{ik} is defined as follows [14]:

$$w_{ik} = 1/\left(d_{ik} + 1\right) \tag{31}$$

where d_{ik} is the spatial Euclidean distance between the kth pixel in neighbors and the central pixel.

Equation (29) presents the updated membership function, in which each cluster's effect is modulated by both the kernel-induced distance and the weighted fuzzy effect of neighboring pixels. This formulation effectively incorporates local spatial structure into the membership update process. Furthermore, Eq. (30) defines the update rule for the cluster centers, based on a kernel-weighted average of the data points, thereby enhancing robustness to noise.

2.8 FRFCM

FRFCM utilizes MR to handle noise in gray-level histograms without dependency on noise type. This algorithm operates on the gray level histogram with an objective function defined [9]:

$$J_{FRFCM} = \sum_{i=1}^{k} \sum_{j=1}^{c} \gamma_i . u_{ij}{}^{q} . \left\| \xi_i - v_j \right\|^2, \quad \sum_{i=1}^{k} \gamma_i = N \tag{32}$$

where ξ_i and q are gray level and the number of gray levels contained in ξ (an image reconstructed by MR), respectively. The membership function and cluster centers are updated by [9]:

$$u_{ij} = \frac{\left\| \xi_i - v_r \right\|^{\frac{-2}{m-1}}}{\sum_{j=1}^{c} \left\| \xi_i - v_j \right\|^{\frac{-2}{m-1}}} \tag{33}$$

$$v_j = \frac{\sum_{i=1}^{k} \gamma_i \left(u_{ij}{}^{q} \xi_i\right)}{\sum_{i=1}^{k} \gamma_i \left(u_{ij}{}^{q}\right)} \tag{34}$$

Also, a median filter enhances the membership function to speed up the convergence and obtain a better membership matrix as follows [9]:

$$u_{ij}^{new} = med\left\{u_{ij}\right\} \tag{35}$$

The membership matrix is updated using inverse distance weighting in the histogram domain, which reduces computational complexity while maintaining segmentation accuracy. The cluster centers are subsequently updated as weighted averages over the histogram bins, where the weights are determined by both the number of pixels with a gray value γ_i and the corresponding membership degrees.

2.9 RFCM

Wang et al. [26] developed RFCM by integrating a residual-driven regularization term into FCM to account for noise characteristics. The objective function is [26]:

$$J_{RFCM} = \sum_{i=1}^{k} \sum_{j=1}^{c} u_{ij}{}^{q} . \left\| x_i - r_i - v_j \right\|^2 + \beta . \Gamma(R) \tag{36}$$

where $\Gamma(R)$ is the regularization term controlled by β (impact of regularization term). For further details on updating terms, such as the membership matrix, cluster centers, and other defined terms in RFCM, refer to [26].

3 Methodology

Traditional FCM-based methods often fail to capture cluster compactness effectively when using Euclidean distance metric, which neglect intra-cluster variations. This limitation presents challenges in image segmentation, particularly for color images. To address these issues, we propose an Improved Gustafson-Kessel (IGK) method. As shown in Fig. 1, our approach first utilizes the gray-level histogram of an image reconstructed through MR, inspired by EnFCM and FRFCM. We replace the Euclidean distance with the Mahalanobis distance and iteratively update cluster centers, the membership matrix, and the positive definite symmetric

matrix. Finally, we apply a median filter to refine the membership partition matrix, achieving effective segmentation in both grayscale and color images with reduced processing time.

3.1 Improved Gustafson-Kessel

Based on the gray-level histogram, we propose the cost function of IGK for image segmentation as follows:

$$J_{IGK} = \sum_{i=1}^{k} \sum_{j=1}^{c} \gamma_i . {u_{ij}}^q . \left(\xi_i - v_j\right)^T . A_j . \left(\xi_i - v_j\right), \quad \sum_{i=1}^{k} \gamma_i = N \tag{37}$$

Using the Lagrange multiplier technique, this equation can be reformulated as an unconstrained optimization problem, minimizing the cost function:

$$\begin{aligned} J_{IGK} = & \sum_{i=1}^{k} \sum_{j=1}^{c} \gamma_i . {u_{ij}}^q . \left(\xi_i - v_j\right)^T . A_j . \left(\xi_i - v_j\right) \\ & - \sum_{i=1}^{k} \lambda_i \left(\sum_{j=1}^{c} u_{ij} - 1\right) \\ & + \sum_{j=1}^{c} \beta_j . \left(det\left(A_j\right) - \rho_j\right) \end{aligned} \tag{38}$$

where λ is the Lagrange multiplier. The partial derivative of J_{IGK} with respect to u_{ij}, equated to zero, yields:

$$\frac{\partial J_{IGK}}{\partial u_{ij}} = q . \gamma_i . u_{ij}^{q-1} . \left(\xi_i - v_j\right)^T . A_j . \left(\xi_i - v_j\right) - \lambda_i = 0 \tag{39}$$

The membership matrix is updated using:

$$u_{ij} = \left(\frac{\left(\xi_i - v_r\right)^T . A_r . \left(\xi_i - v_r\right)}{\sum_{j=1}^{c} \left(\xi_i - v_j\right)^T . A_j . \left(\xi_i - v_j\right)} \right)^{1/q-1} \tag{40}$$

Similarly, the cluster centers are derived by differentiating J_{IGK} with respect to v_j:

$$\frac{\partial J_{IGK}}{\partial v_j} = -2 \sum_{i=1}^{k} \gamma_i . {u_{ij}}^q . \left(\xi_i - v_j\right) . A_j = 0 \tag{41}$$

$$v_j = \frac{\sum_{i=1}^{k} \gamma_i . {u_{ij}}^q . \xi_i}{\sum_{i=1}^{k} \gamma_i . {u_{ij}}^q} \tag{42}$$

Finally, the partial derivative with respect to A_j gives:

$$\begin{aligned} \frac{\partial J_{IGK}}{\partial A_j} = & \sum_{i=1}^{k} \gamma_i . {u_{ij}}^q . \left(\xi_i - v_j\right)^T . \left(\xi_i - v_j\right) \\ & - \sum_{i=1}^{k} \left(\lambda_i . \frac{\partial}{\partial A_j} \left(det\left(A_j\right)\right)\right) \\ = & \sum_{i=1}^{k} \gamma_i . {u_{ij}}^q . \left(\xi_i - v_j\right)^T . \left(\xi_i - v_j\right) \\ & - \sum_{i=1}^{k} \left(\lambda_i . {u_{ij}}^q . A_j^{-1}\right) = 0 \end{aligned} \tag{43}$$

Solving Eq. 43, we obtain:

$$F_i = \frac{\sum_{i=1}^{k} \gamma_i . {u_{ij}}^q . \left(\xi_i - v_j\right)^T . \left(\xi_i - v_j\right)}{\sum_{i=1}^{k} {u_{ij}}^q} \tag{44}$$

$$A_j = \lambda_i . \left(det\left(F_i\right)\right)^{\frac{1}{n}} . F_i^{-1} \tag{45}$$

Based on the obtained equations, the pseudocode of proposed IGK algorithm has been illustrated in Algorithm 1.

3.2 Morphological Reconstruction (MR)

The convergence rate of FCM and GK algorithms depends on data distribution properties, making them susceptible to noise and yielding suboptimal segmentation results in noisy images [9]. MR serves as a robust tool for image processing tasks including filtering, segmentation, and feature extraction [34]. As illustrated in Fig. 2, MR improves data distribution without prior knowledge of noise type and outperforms mean and median filtering by preserving object contours while reducing noise. In our approach (Fig. 1), MR optimizes data distribution before clustering. We employ a 3×3 square structuring element (SE) with the fast grayscale reconstruction (FGR) algorithm [35]. Dilation and erosion operations are two basic morphological reconstruction operations [28].

Grayscale reconstruction by the dilation operator $D_I^{(1)}(f)$ with a flat SE K is defined as:

$$D_I^{(1)}(f) = (f \oplus K) \wedge I \tag{46}$$

where I and f are original grayscale image and marker image ($f \leq I$), respectively. Also, $\wedge$ operation stands for the pointwise minimum.

The grayscale reconstruction by erosion operator $E_I^{(1)}(f)$ with a flat SE K is defined as:

$$E_I^{(1)}(f) = (f \ominus K) \vee I \tag{47}$$

where I and f are original grayscale image and marker image ($f \geq I$), respectively. Also, $\vee$ operation stands for the pointwise maximum.

Closing $C_I^{(1)}(f)$ and opening $O_I^{(1)}(f)$ operations based on dilation and erosion provide enhanced filtering capabilities compared to basic morphological operations [34]. The closing operation effectively smooths texture details [9]. These morphological reconstructions are defined as follows:

$$C_I^{(1)}(f) = E_I^{(1)}\left(D_I^{(1)}(f)\right) \tag{48}$$

$$O_I^{(1)}(f) = D_I^{(1)}\left(E_I^{(1)}(f)\right) \tag{49}$$

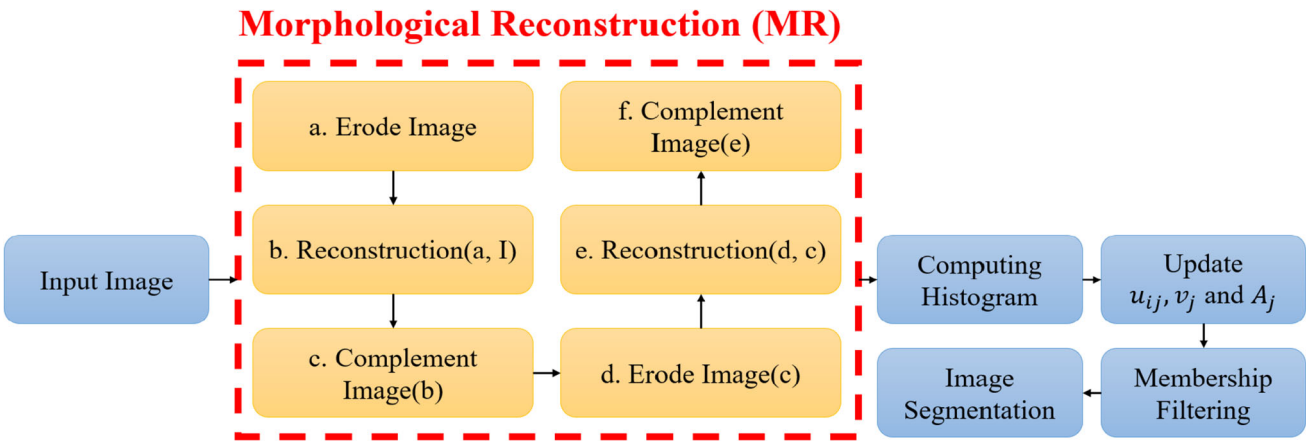

Fig. 1 Block-diagram of the proposed algorithm for image segmentation

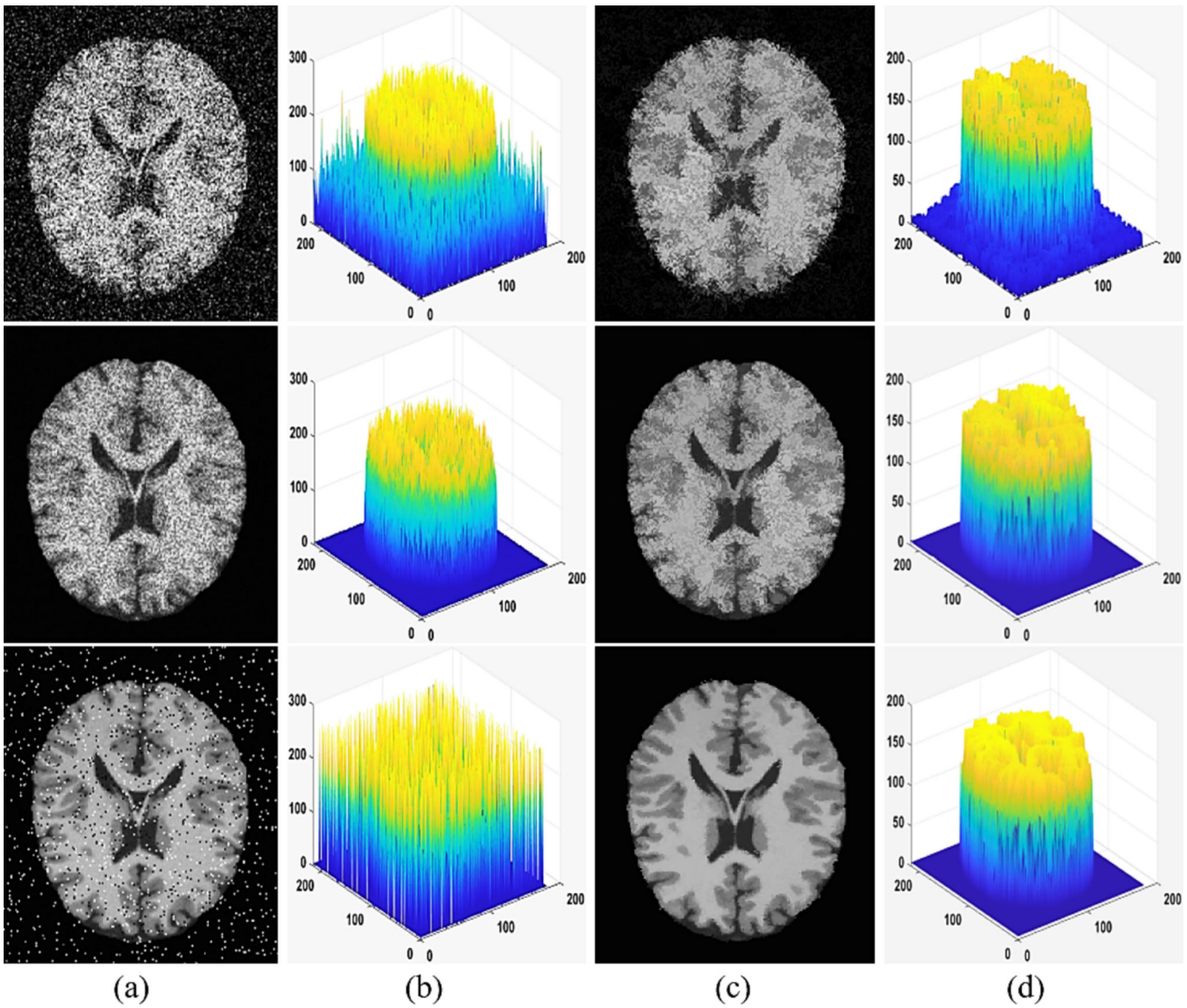

Fig. 2 Comparison of MR method in noise removal: (a) Images with Gaussian noise (the mean value is zeros and the variance is 5%), Speckle noise with density 5%, and Salt & Pepper noise with density 5%. (b) Data distribution of noisy images. (c) MR-filtered images. (d) Data distribution post-MR

Algorithm 1 Improved Gustafson-Kessel Algorithm for Image Segmentation

Require: Observed image X, constructed the new image ξ, number of clusters c, fuzzification exponent q, filter window w and threshold η.
Output: Segmented image
1: Initialize membership matrix
2: Set $t \leftarrow 0$
3: Compute cluster centers:
$v_j = \frac{\sum_{i=1}^{k} \gamma_i . u_{ij}{}^q . \xi_i}{\sum_{i=1}^{k} \gamma_i . u_{ij}{}^q}$
4: **repeat**
5: **for** $i \leftarrow 1$ to c **do**
6: Compute fuzzy covariance matrix:
$F_i = \frac{\sum_{i=1}^{k} \gamma_i . u_{ij}{}^q . (\xi_i - v_j)^T . (\xi_i - v_j)}{\sum_{i=1}^{k} u_{ij}{}^q}$
7: Compute normalized metric matrix:
$A_j = \lambda_i . \left(det(F_i)\right)^{\frac{1}{n}} . F_i{}^{-1}$
8: **end for**
9: **for** $j \leftarrow 1$ to N **do**
10: **for** $i \leftarrow 1$ to c **do**
11: Compute distance:
12: $D_{ij}{}^2 \leftarrow \left(\xi_i - v_j\right)^T . A_j . \left(\xi_i - v_j\right)$
13: **end for**
14: **for** $i \leftarrow 1$ to c **do**
15: Update membership:
16: $u_{ij} = \left(\frac{(\xi_i - v_r)^T . A_r . (\xi_i - v_r)}{\sum_{j=1}^{c} (\xi_i - v_j)^T . A_j . (\xi_i - v_j)} \right)^{1/q-1}$
17: **end for**
18: **end for**
19: Compute $\Delta U \leftarrow \max\{U^{(It)} - U^{(It+)}\}$
20: $t \leftarrow t + 1$
21: **until** $\Delta U < \eta$ or $t \geq max\_iter$
22: **for** $j \leftarrow 1$ to N **do**
23: **for** $i \leftarrow 1$ to c **do**
24: Compute distance:
25: $D_{ij}{}^2 \leftarrow \left(X_i - v_j\right)^T . A_j . \left(X_i - v_j\right)$
26: **end for**
27: **for** $i \leftarrow 1$ to c **do**
28: Update membership:
$U_{ij} = \left(\frac{(X_i - v_r)^T . A_r . (X_i - v_r)}{\sum_{j=1}^{c} (X_i - v_j)^T . A_j . (X_i - v_j)} \right)^{1/q-1}$
29: **end for**
30: **end for**
31: Apply Median Filter on U_{ij}
32: Return cluster centers, membership matrix and covariance matrix.

4 Experimental Results

This section presents experimental results for grayscale and color image segmentation using the proposed IGK algorithm. We compare IGK with established FCM-based methods such as FCM [29], GK [33], ENFCM [11], FGFCM [12], FLICM [13], ARKFCM [17], FRFCM [9], and RFCM [26], providing both visual and quantitative analyses. Experiments were conducted on an ACER desktop with an Intel Core i7–9750H CPU at 2.60 GHz and 16 GB RAM.

To evaluate segmentation performance, we employed four metrics: Segmentation Accuracy (*SA*) [36], Dice Similarity (*DS*), Jaccard Similarity (*JS*), and Contour Matching Score (*CS*) [37]. SA is defined as the proportion of correctly segmented pixels:

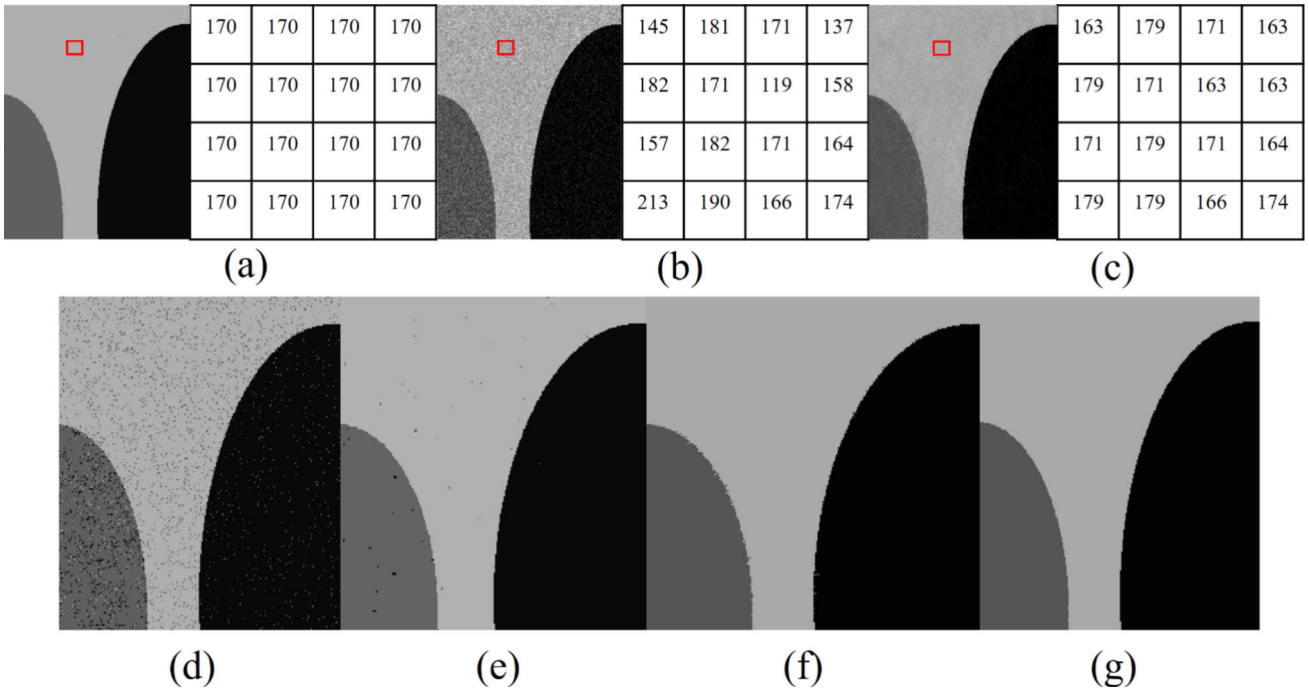

Fig. 3 Ablation study results demonstrating IGK performance under different preprocessing conditions. (a) Original image. (b) Gaussian noise-corrupted image. (c) Result after applying MR. (d) Segmentation result using IGK without MR and without median filtering. (e) Segmentation result using IGK with median filtering but without MR. (f) Segmentation result using IGK with MR but without median filtering. (g) Segmentation result using **IGK** with both MR and median filtering

$$SA = \sum_{k=1}^{c} \frac{A_k \cap B_k}{A_k \cup B_k} \tag{50}$$

where A_k and B_k are the set of pixels belonging to the kth cluster segmented by the proposed algorithm and the set of pixels belonging to the cluster in the Ground Truth (GT).

DS index is used to assess the overlap degree between two images, including segmented image and GT. *JS* index is used to measure the similarity between two images. *CS* index is used to evaluate the contour matching score between the segmented image and GT. This index is in the range of [0,1], where a score of 1 indicates a perfect match.

$$DS\,(A,\,B) = \frac{2\,|A \cap B|}{|A| + |B|} \tag{51}$$

$$JS\,(A,\,B) = \frac{|A \cap B|}{|A \cup B|} \tag{52}$$

$$CS = \frac{2.P^c.R^c}{P^c + R^c} \tag{53}$$

where P^c and R^c are precision and recall, respectively.

4.1 Data Description

We evaluated the performance of the proposed IGK algorithm on both grayscale and color images. For grayscale evaluation, we first used two synthetic 256×256 images are (see Fig. 3 and 4). The first image contains three intensity values (0, 85, and 170), while the second image has four intensity values (0, 85, 170, and 255). Subsequently, we used three MRI images highlighting multiple sclerosis (MS) lesions (Fig. 5) to demonstrate IGK's effectiveness in medical applications.

For color image segmentation, we utilized images from four datasets : BSDS500 (Berkeley Segmentation Dataset) [38], MSRC (Microsoft Research Cambridge) [39], SUT (orthogonal facial color images for facial reconstruction) [40], and fused MRI images from the BrainWeb dataset (a simulated brain database) [41] with dimensions of 181×217 (see Fig. 7–12).

4.2 Parameter Setting

The numerical implementation of IGK and the other algorithms requires the setting of several constant parameters. Three essential parameters were used across all algorithms: fuzzy exponent q=2, minimal error threshold $\eta = 10^{-5}$, and maximal number of iterations 50. For IGK and other applicable algorithms, we used a 3×3 square SE for MR and a window 3× 3 for membership matrix filtering. For the EnFCM, we experimentally set $\alpha = 4.2$, to control the influence of neighboring terms. In FGFCM, spatial scale factor

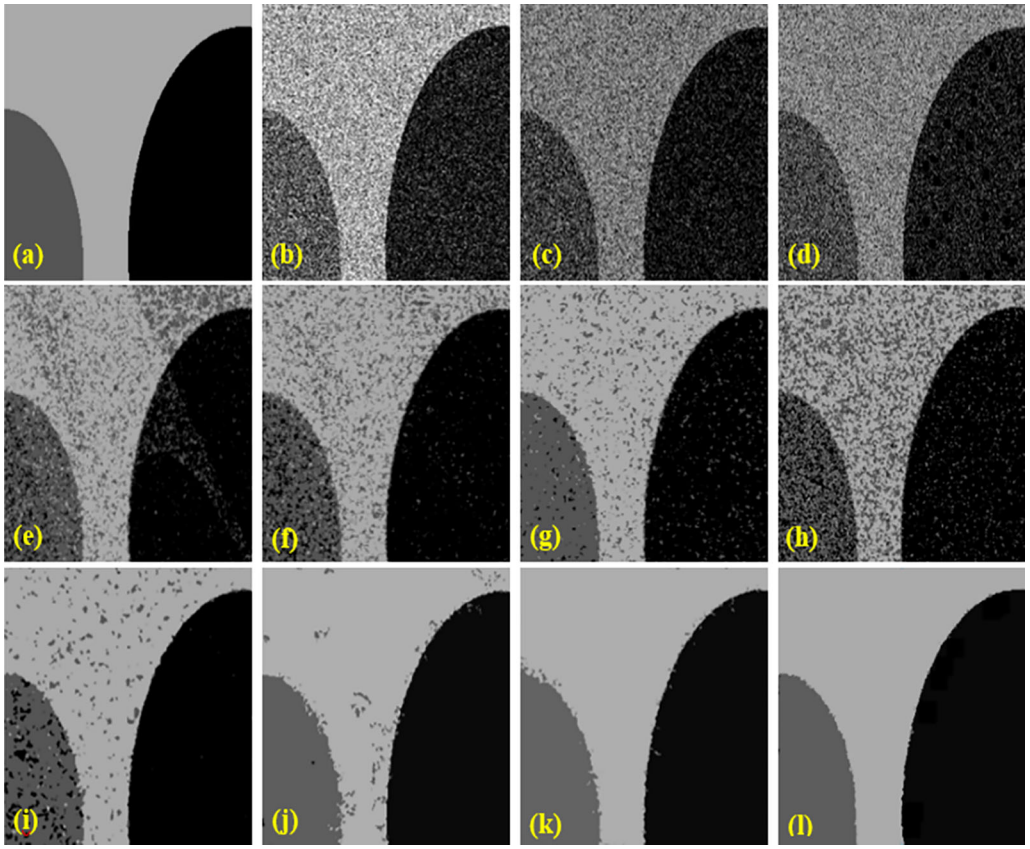

Fig. 4 Comparison of segmentation results on the first synthetic image. (a) Original image. (b) Noisy image (Gaussian noise with zero mean and 10% variance). (c) Segmentation result using FCM algorithm. (d) Segmentation result using GK algorithm. (e) Segmentation result using EnFCM algorithm. (f) Segmentation result using FGFCM algorithm. (g) Segmentation result using FLICM algorithm. (h) Segmentation result using ARKFCM algorithm. (i) Segmentation result using KWFLICM algorithm. (j) Segmentation result using RFCM algorithm. (k) Segmentation result using FRFCM algorithm. (l) Segmentation result using **IGK** algorithm

and grayscale factor were $\lambda_s = 3$ and $\lambda_g = 6$, respectively. Except the mentioned indispensable parameters and the number of cluster center, there is no other parameters for FLICM, ARKFCM, and KWFLICM. For RFCM, the parameter controlling the decreasing rate of weighting matrix, the ξ parameter, was set to ξ=*0.0008*. The standard deviation of image data is related to noise levels in RFCM. Therefore, the β parameter is set in virtue of the standard deviation of each channel. A constant 3×3 window size was used across all the algorithms except FCM and GK for fair comparison.

4.3 Results on Synthetic Images

Synthetic images offer advantages for algorithm evaluation through prior knowledge of image types and control over parameters like modality and noise, making it easier to evaluate algorithm performance objectively reason, synthetic images were chosen to initially validate the proposed IGK algorithm [24]. We used the grayscale synthetic images shown in Fig. 3(a) and 5(b), corrupted with different noise types: Gaussian noise (GN), salt and pepper noise (SPN), and speckle noise (SN). These noisy versions were used to assess and compare segmentation performance across various algorithms. Fig. 3(c-l) and 4(c-l) display the segmentation outcomes for IGK and the compared algorithms. Each algorithm was run ten times, with the best performance selected for comparison.

As illustrated in Algorithm 1, the proposed IGK algorithm applies MR operation as a preprocessing step and median filtering after updating the membership matrix. Fig. 3 demonstartes the performance of IGK under different configurations to evaluate the individual contributions of these components. Without MR operation and median filtering (Fig. 3(d)), segmentation lacks spatial consistency as noise and irregular intensity variations mislead the clustering process. MR operation enhances robustness in low-contrast regions and improves edge preservation Fig. 3(c), while median filtering eliminates scattered noise in the membership function and improves spatial coherence. Together, these components significantly the robustness of the proposed IGK algorithm by

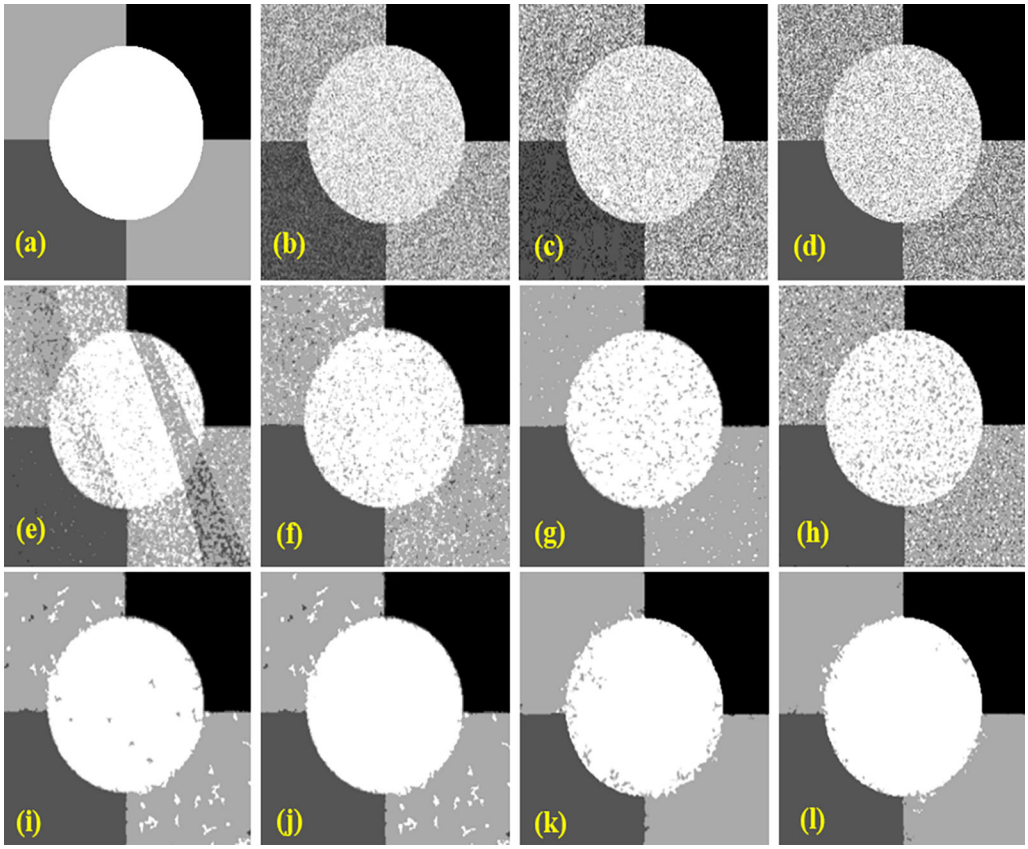

Fig. 5 Comparison of segmentation results on the second synthetic image. (a) Original image. (b) Noisy image (Speckle noise with 10% variance). (c) Segmentation result using FCM algorithm. (d) Segmentation result using GK algorithm. (e) Segmentation result using EnFCM algorithm. (f) Segmentation result using FGFCM algorithm. (g) Segmentation result using FLICM algorithm. (h) Segmentation result using ARKFCM algorithm. (i) Segmentation result using KWFLICM algorithm. (j) Segmentation result using RFCM algorithm. (k) Segmentation result using FRFCM algorithm. (l) Segmentation result using **IGK** algorithm

addressing structural guidance and local consistency requirements.

As shown in Fig. 4, algorithms like FCM, GK, EnFCM, FGFCM, and ARKFCM showed limited noise immunity, leading to suboptimal segmentation under GN. These algorithms are notably sensitive to GN. However, FLICM and KWFLICM, which incorporate criterion-free local information and kernel coefficients, exhibited better noise immunity and outperformed the aforementioned algorithms in segmenting GN-corrupted images. RFCM, FRFCM, and IGK also showed strong performance under GN. Fig. 4(j-l) illustrate that IGK, in particular, demonstrated high noise removal effectiveness and preserved image edges better than RFCM and FRFCM.

Similarly, in Fig. 5, FLICM, RFCM, FRFCM, and IGK performed well under SN, whereas other algorithms remained sensitive to SN. In the second synthetic image, IGK outperformed FLICM, RFCM, and FRFCM, attributed to its new similarity measure supporting more compact clusters. As shown in Fig. 5, increasing the number of cluster centers diminished segmentation efficiency in FCM-based algorithms, but IGK addressed this issue by applying Mahalanobis distance instead of Euclidean distance, effectively preserving edges across different noise types.

Tables 1 and 2 show that IGK's SA criterion surpasses that of other algorithms across different noise types, indicating effective noise immunity and detail preservation. This improvement stems from IGK's use of membership matrix filtering and MR. KWFLICM employs a kernel metric to address FLICM's detail preservation challenges, yielding good segmentation under GN and SPN, but struggling with SN. Both IGK and FRFCM enhance noise immunity through MR and membership matrix filtering. However, FRFCM's reliance on Euclidean distance weakens its performance as cluster centers increase, especially under varied noise. IGK, utilizing Mahalanobis distance, maintains effective edge preservation and segmentation performance under diverse noise conditions. While GK and FGFCM perform well under SPN and ENFCM under SN, FLICM shows efficiency with a low number of clusters for SN and for GN with higher clus-

Table 1 Segmentation accuracy (↑SA%) of different algorithms on the first synthetic image with different noises

Noise	FCM	GK	EnFCM	FGFCM	FLICM	ARKFCM	KWFLICM	RFCM	FRFCM	IGK
Gaussian 5%	66.25	78.52	91.10	95.75	98.01	72.23	99.55	99.02	99.36	**99.57**
Gaussian 10%	65.32	76.61	86.53	85.12	91.43	67.42	94.14	85.83	98.24	**98.92**
Gaussian 15%	64.56	72.81	82.36	80.20	79.53	62.12	84.21	80.12	85.74	**87.38**
Salt & Pepper 10%	94.21	96.15	92.31	96.39	93.41	79.23	**99.98**	99.33	99.48	99.93
Salt & Pepper 20%	86.24	88.61	86.53	92.82	82.18	75.17	99.84	99.31	99.83	**99.86**
Salt & Pepper 30%	80.36	82.95	79.82	86.65	76.24	72.53	99.62	99.29	99.70	**99.77**
Speckle 10%	75.16	81.08	94.86	97.57	98.13	78.20	99.55	99.11	99.44	**99.64**
Speckle 20%	72.81	78.16	90.21	91.83	**95.83**	69.18	92.13	83.94	91.44	95.54
Speckle 30%	70.14	73.82	84.45	84.32	**90.70**	72.41	80.88	81.25	82.84	81.23

Table 2 Segmentation accuracy (↑SA%) of different algorithms on the second synthetic image with different noises

Noise	FCM	GK	EnFCM	FGFCM	FLICM	ARKFCM	KWFLICM	RFCM	FRFCM	IGK
Gaussian 5%	40.67	44.22	88.24	93.84	97.64	84.23	95.67	98.69	99.21	**99.51**
Gaussian 10%	33.56	35.80	81.68	83.25	90.39	78.76	84.62	82.41	97.73	**98.16**
Gaussian 15%	30.72	33.61	74.65	77.21	78.60	68.97	80.23	79.12	95.23	**97.53**
Salt & Pepper 10%	81.39	84.71	87.43	94.22	91.78	84.17	99.68	99.15	99.90	**99.91**
Salt & Pepper 20%	75.42	78.48	76.36	88.47	81.06	82.78	99.52	99.12	**99.80**	99.77
Salt & Pepper 30%	64.19	68.05	68.71	80.38	72.41	75.92	99.04	99.02	98.73	**99.65**
Speckle 10%	50.81	55.12	83.92	91.68	96.15	66.43	96.54	97.01	97.85	**98.28**
Speckle 20%	42.67	46.39	77.84	81.68	81.45	63.21	80.42	80.13	84.82	**85.19**
Speckle 30%	34.48	36.61	71.85	75.27	78.74	59.81	72.26	79.19	79.45	**80.43**

Table 3 Comparison of clustering centers produced by different algorithms

Methods	The First Synthesis Image (Gaussian noise with zero mean and 10% variance)		The Second Synthesis Image (Speckle noise with 10% variance)	
	Values of cluster centers	RMSE↓	Values of cluster centers	RMSE↓
FCM	(12.7, 118.63, 224.76)	37.78	(3.47, 100.39, 171.72, 247.02)	8.89
GK	(6.63, 103.73, 218.69)	30.36	(0.02, 92.86, 175.48, 249.75)	5.46
EnFCM	(34.61, 111.69, 169.35)	25.23	(19.87, 99.83, 167.07, 215.26)	23.46
FGFCM	(28.36, 111.32, 175.67)	22.58	(0.20, 88.29, 167.42, 223.76)	15.76
FLICM	(8.89, 94.26, 183.85)	10.90	(0.38, 85.73, 165.97, 232.85)	11.26
ARKFCM	(12.00, 37.89, 167.12)	28.12	(0.41, 86.30, 171.08, 228.49)	13.28
KWFLICM	(7.31, 93.78, 181.42)	9.33	(0.71, 86.63, 176.02, 245.87)	5.54
RFCM	(29.21, 112.58, 176.17)	23.47	(0.64, 88.79, 173.65, 243.15)	6.49
FRFCM	(9.40, 96.78, 173.77)	8.97	(0.14, 86.60, 171.35, 244.85)	5.18
IGK	(8.42, 85.29, 168.27)	**4.97**	(1.36e-29, 85.78, 169.57, 248.48)	**3.29**

ter counts. ARKFCM demonstrates poor performance across noise types. In summary, RFCM, FRFCM, and IGK show the best overall efficiency in noisy image segmentation, with IGK being notably robust even as cluster centers increase.

Table 3 provides a detailed comparison of clustering center values across different algorithms using the Root Mean Square Error (*RMSE*) of clustering centers to assess performance.

In the first synthetic image, IGK achieves notable clustering accuracy, with the lowest RMSE values for key clustering centers, indicating closer approximation to true values. Specifically, IGK achieves a value of 8.42 for the first clustering center, with the best values for the second (85.29, closest to 85) and third clustering centers (168.27) as well. In the second synthetic image, IGK also demonstrates superior performance, achieving the lowest RMSE for clustering cen-

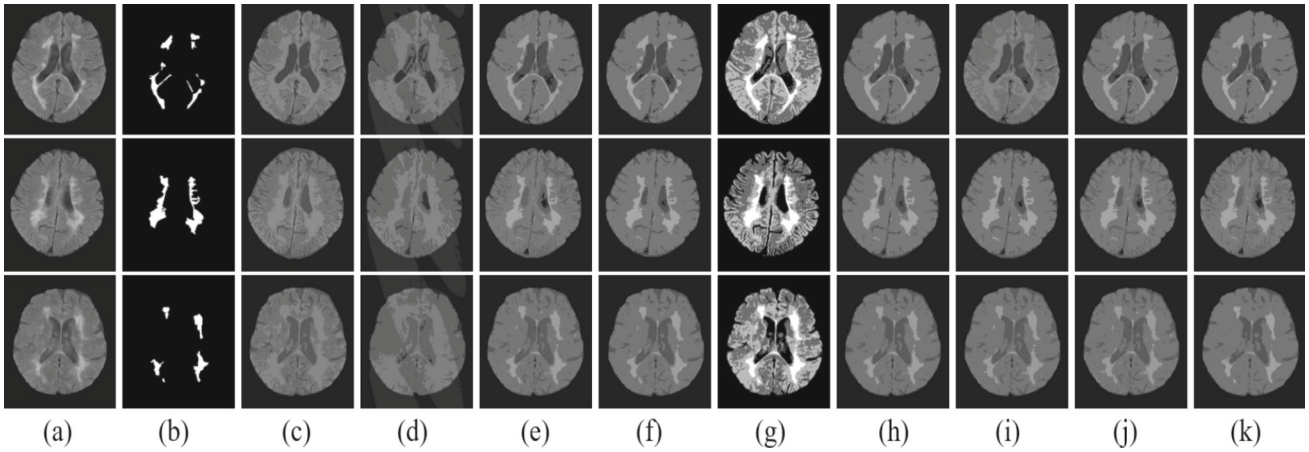

Fig. 6 Comparison of segmentation results on MS defect images (c=4). (a) Original MS MRI images. (b) Ground truth images, manually segmented by a radiologist. (c) GK algorithm results. (d) EnFCM algorithm results. (e) FGFCM algorithm results. (f) FLICM algorithm results. (g) ARKFCM algorithm results. (h) KWFLICM algorithm results. (i) RFCM algorithm results. (j) FRFCM algorithm results. (k) **IGK** algorithm results

Table 4 Segmentation performance (%) of different algorithms on MS defect images

Algorithm	Fig. 6, Row 1			Fig. 6, Row 2			Fig. 6, Row 3		
	SA↑	Dice↑	Jaccard↑	SA↑	Dice↑	Jaccard↑	SA↑	Dice↑	Jaccard↑
GK	85.39	28.06	16.32	91.61	51.91	35.05	87.53	29.36	17.21
EnFCM	81.00	23.07	13.04	86.96	40.98	25.77	81.01	21.42	12.00
FGFCM	98.73	81.74	69.12	**99.53**	**94.87**	**90.24**	98.26	74.83	59.79
FLICM	99.28	88.74	79.76	99.47	94.34	89.29	97.52	77.73	63.58
ARKFCM	99.28	88.66	79.67	99.44	93.54	87.88	98.83	81.47	68.73
KWFLICM	99.10	86.26	75.85	99.38	93.50	87.80	98.40	76.37	61.77
RFCM	86.20	29.22	17.11	99.24	92.12	85.39	98.06	72.75	57.17
FRFCM	98.50	79.08	65.40	99.42	93.84	88.39	98.02	72.33	56.65
IGK	**99.59**	**91.76**	**85.78**	99.48	94.39	89.37	**99.34**	**88.52**	**81.49**

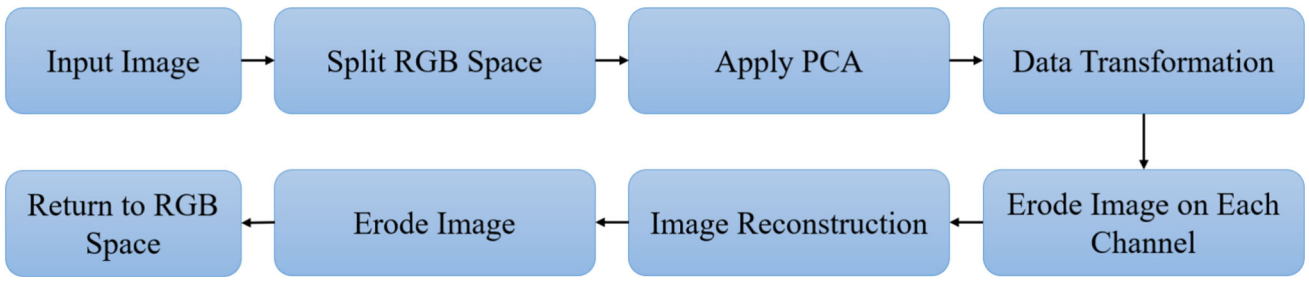

Fig. 7 Block-diagram of MMR for color image reconstruction

Table 5 Segmentation performance (%) of various algorithms on BSDS500 images

Algorithm	Fig. 7, Row 1			Fig. 7, Row 2			Fig. 7, Row 3			Fig. 7, Row 4			Fig. 7, Row 5		
	CS↑	DS↑	JS↑	CS↑	DS↑	JS↑	CS↑	DS↑	JS↑	CS↑	DS↑	JS↑	CS↑	DS↑	JS↑
RFCM	18.33	39.55	24.65	31.65	52.67	39.84	45.16	64.83	47.96	**92.67**	94.40	89.40	97.79	98.20	96.46
FRFCM	16.80	39.40	24.54	28.25	52.19	35.40	44.36	65.65	48.87	87.77	93.35	87.53	59.87	95.14	90.73
IGK	**98.79**	**97.93**	**95.95**	**50.72**	**78.77**	**64.76**	**70.20**	**73.21**	**57.74**	91.72	**94.77**	**90.07**	**98.69**	**98.24**	**96.64**

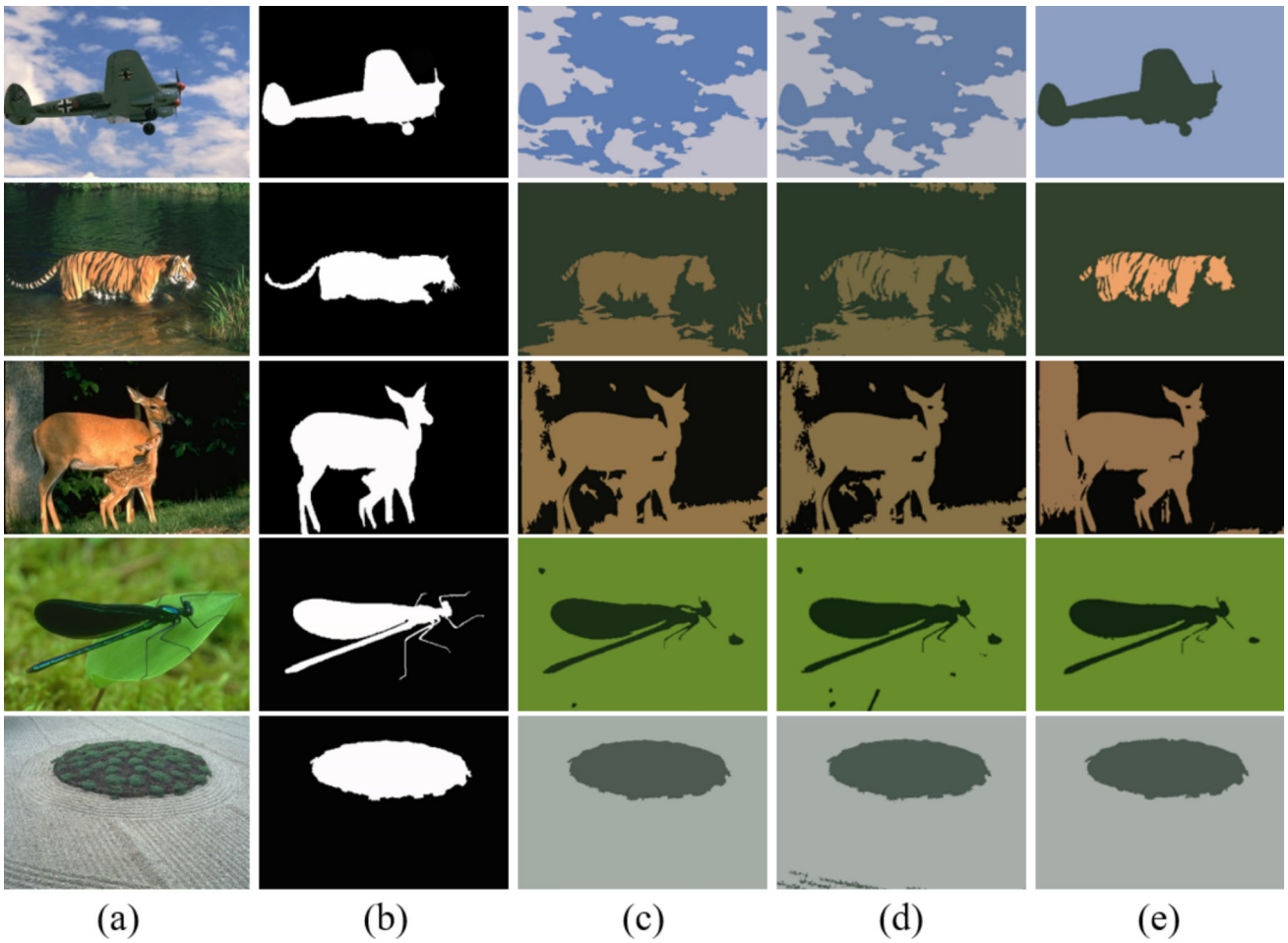

Fig. 8 Comparison of segmentation results on color images from BSDS500 (*c=2*). (a) Original images. (b) Ground truth. (c) FRFCM results. (d) RFCM results. (e) IGK results

Table 6 Segmentation performance (%) of various algorithms on MSRC images

Algorithm	Fig. 8, Row 1			Fig. 8, Row 2			Fig. 8, Row 3			Fig. 8, Row 4			Fig. 8, Row 5		
	CS↑	DS↑	JS↑	CS↑	DS↑	JS↑	CS↑	DS↑	JS↑	CS↑	DS↑	JS↑	CS↑	DS↑	JS↑
RFCM	50.25	88.99	80.17	23.22	75.05	60.07	79.57	96.75	93.71	68.07	91.08	83.62	12.25	34.04	20.51
FRFCM	50.90	89.11	80.36	28.44	75.20	60.26	73.14	96.05	92.40	66.11	91.62	84.53	11.45	33.56	20.16
IGK	**78.49**	**96.77**	**93.74**	**71.01**	**94.38**	**89.36**	**84.55**	**96.95**	**94.09**	**94.90**	**97.84**	**95.78**	**16.60**	**62.43**	**45.38**

Table 7 Segmentation performance (%) of various algorithms on SUT images for facial skin segmentation

Algorithm	Fig. 9, Col 1			Fig. 9, Col 2			Fig. 9, Col 3			Fig. 9, Col 4			Fig. 9, Col 5		
	CS↑	DS↑	JS↑	CS↑	DS↑	JS↑	CS↑	DS↑	JS↑	CS↑	DS↑	JS↑	CS↑	DS↑	JS↑
FRFCM	55.95	85.93	75.33	52.17	88.08	78.71	26.21	73.39	57.97	16.83	64.05	47.11	**73.46**	95.82	91.98
RFCM	59.07	86.46	76.14	53.90	88.52	79.40	24.52	74.07	58.82	17.75	65.84	49.08	72.26	**95.85**	**92.04**
IGK	**75.10**	**95.31**	**91.02**	**72.90**	**95.97**	**92.25**	**77.07**	**96.88**	**93.95**	**84.94**	**97.56**	**95.23**	73.03	95.78	91.91

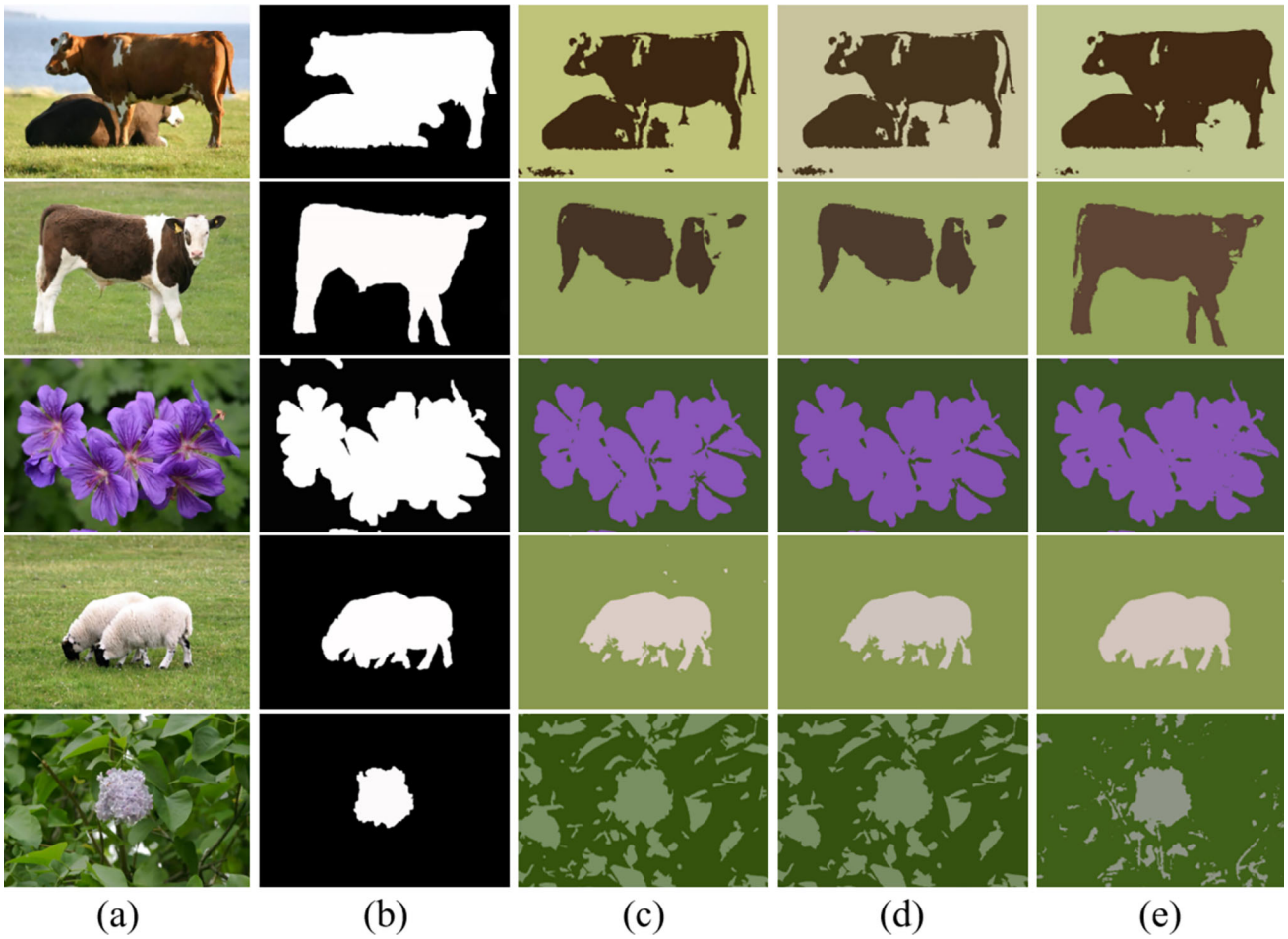

Fig. 9 Comparison of segmentation results on color images from MSRC (c=2). (a) Original images. (b) Ground truth. (c) FRFCM results. (d) RFCM results. (e) IGK results

Table 8 Segmentation performance (%) of various algorithms on fused MRI images

Algorithm (WM)	Fig. 10, Row 1			Fig. 10, Row 2			Fig. 10, Row 3			Fig. 10, Row 4			Fig. 10, Row 5		
	CS↑	DS↑	JS↑	CS↑	DS↑	JS↑	CS↑	DS↑	JS↑	CS↑	DS↑	JS↑	CS↑	DS↑	JS↑
FRFCM	**91.20**	**89.93**	**81.70**	95.48	94.53	89.64	95.86	96.13	92.70	97.97	96.77	93.73	**96.11**	95.12	90.70
RFCM	80.03	84.33	72.91	93.54	95.03	90.53	95.30	95.93	92.17	84.63	93.84	88.40	87.95	94.69	89.92
IGK	86.38	87.36	77.56	**97.34**	**96.65**	**93.52**	**96.19**	**96.42**	**92.86**	**98.89**	**97.13**	**94.43**	94.68	**95.28**	**90.98**
Algorithm (GM)	Fig. 10, Row 1			Fig. 10, Row 2			Fig. 10, Row 3			Fig. 10, Row 4			Fig. 10, Row 5		
	CS↑	DS↑	JS↑	CS↑	DS↑	JS↑	CS↑	DS↑	JS↑	CS↑	DS↑	JS↑	CS↑	DS↑	JS↑
FRFCM	83.14	**72.85**	52.79	81.13	72.94	57.40	90.98	86.66	**78.04**	88.78	87.19	77.28	88.29	86.13	75.63
RFCM	73.39	63.36	46.37	79.36	74.37	59.19	86.75	83.62	71.85	77.56	82.19	69.76	90.39	84.36	72.95
IGK	**83.29**	69.56	**53.32**	**91.17**	**86.66**	**76.45**	**91.03**	**87.13**	75.64	**90.10**	**88.33**	**79.10**	**91.77**	**86.45**	**75.81**
Algorithm (CSF)	Fig. 10, Row 1			Fig. 10, Row 2			Fig. 10, Row 3			Fig. 10, Row 4			Fig. 10, Row 5		
	CS↑	DS↑	JS↑	CS↑	DS↑	JS↑	CS↑	DS↑	JS↑	CS↑	DS↑	JS↑	CS↑	DS↑	JS↑
FRFCM	62.35	62.23	45.17	29.11	46.42	30.22	78.36	**81.45**	**68.71**	68.99	76.27	61.64	73.23	70.83	54.83
RFCM	19.58	32.83	19.64	30.26	46.89	30.63	30.35	56.83	39.70	19.32	43.78	28.03	92.53	75.81	61.05
IGK	**62.89**	**62.31**	**45.24**	**84.32**	**83.46**	**71.62**	**79.53**	79.91	66.54	**75.24**	**79.79**	**66.37**	**87.28**	**79.10**	**65.43**

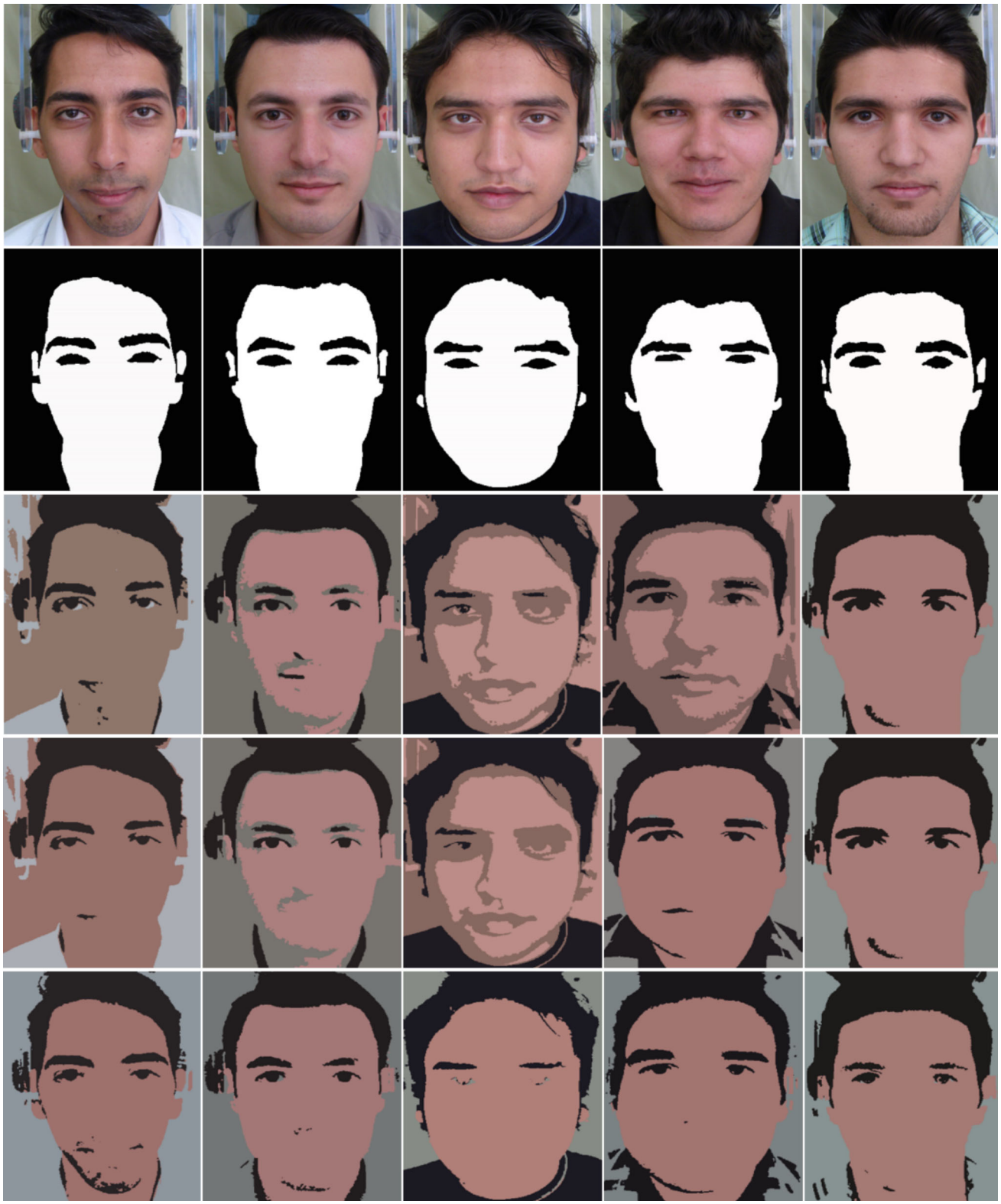

Fig. 10 Comparison of segmentation results on color images from SUT (c=*3*). (Row 1) Original images. (Row 2) Ground truth. (Row 3) FRFCM results. (Row 3) RFCM results. (Row 4) IGK results

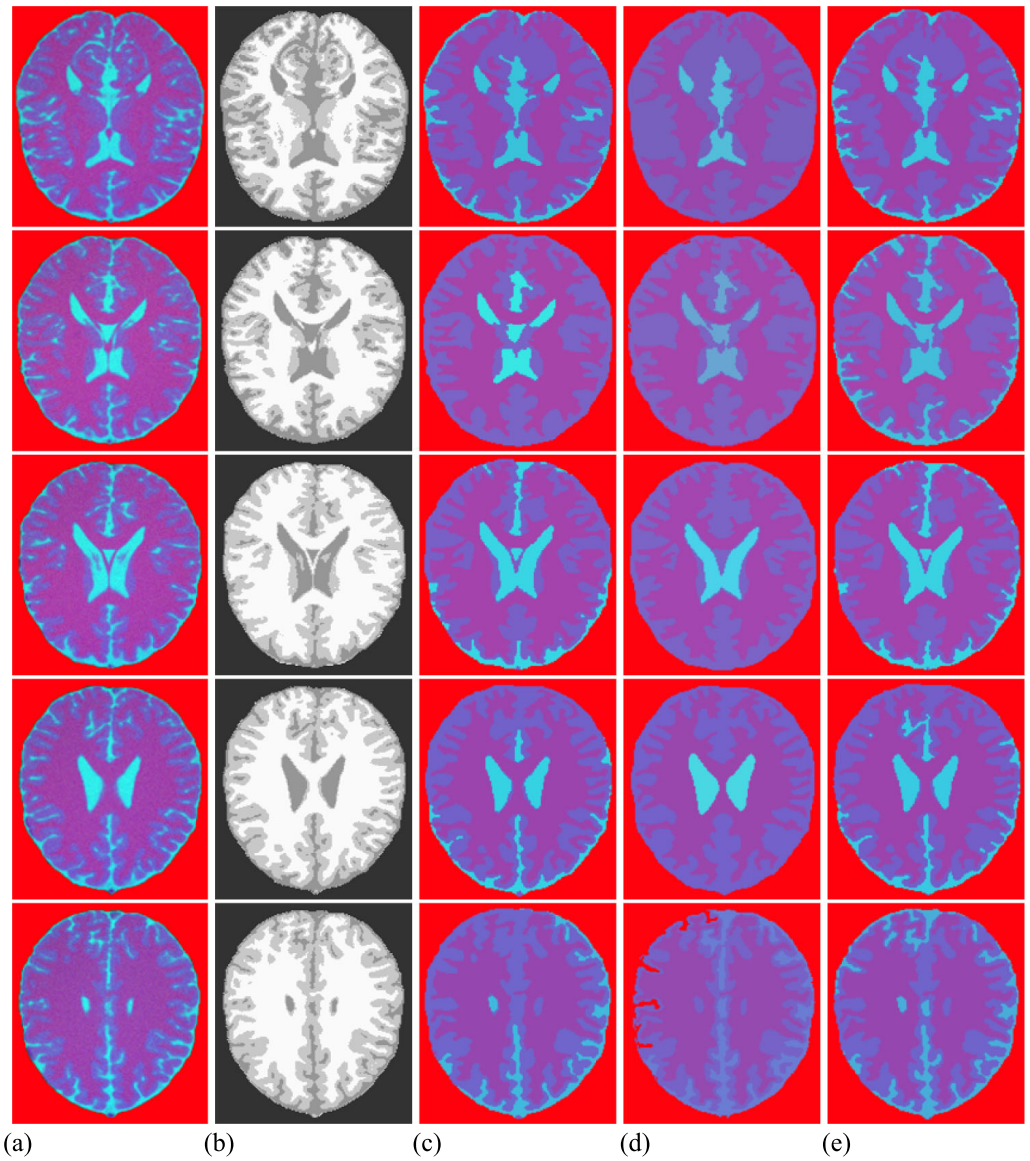

Fig. 11 Comparison of segmentation results on fused MRI images (*c=4*). (a) Original images. (b) Ground truth. (c) FRFCM results. (d) RFCM results. (e) IGK results

ters across different noise types. For instance, IGK obtains 1.36e-29 for the first clustering center, among the best values for the second (85.78), third (169.57), and fourth clustering centers (248.48). Overall, IGK's RMSE (3.29) is the lowest among all compared algorithms for the second synthetic image, indicating precise clustering. These results suggest that IGK's use of MR, membership matrix filtering, and Mahalanobis distance significantly enhances clustering accuracy, particularly under noisy conditions, making it effective for accurate image segmentation.

4.4 Results on Medical Images

Multiple sclerosis (MS) is a chronic neurodegenerative disorder affecting the central nervous system, marked by progressive myelin damage around neurons. MRI plays a crucial role in MS diagnosis by revealing MS lesions and assessing brain component volumes such as white matter (WM), gray matter (GM), and cerebrospinal fluid (CSF). Effective segmentation of these lesions is vital for both diagnosis and disease monitoring over time [42–44]. To evaluate IGK's performance on medical images, three representative T2-weighted MRI scans from MS patients, sourced from the Golgasht Medical Imaging Center (GMIT) in Tabriz, Iran, were analyzed. Standardized protocols for MRI scanning

Fig. 12 Comparison of segmentation results on color images from BSDS500. (a) Original images. (b) FRFCM results (c=2). (c) RFCM results (c=2). (d) IGK results (c=2). (e) FRFCM results (c=3). (f) RFCM results (c=3). (g) IGK results (c=3)

Table 9 Execution times of various algorithms on grayscale images (seconds)

Image	FCM	GK	EnFCM	FGFCM	FLICM	ARKFCM	KWFLICM	RFCM	FRFCM	IGK
Fig. 3	0.63	0.16	0.14	0.46	128.46	2.43	51.10	3.8	**0.06**	**0.07**
Fig. 4	1.24	0.22	0.13	0.46	151.23	3.01	50.14	3.21	**0.05**	**0.06**
Fig. 5, Row 1	5.22	0.98	0.95	2.22	952.12	17.08	241.02	46.54	**0.14**	**0.15**
Fig. 5, Row 2	6.38	1.34	0.98	2.20	918.90	16.98	600.10	16.06	**0.12**	**0.13**
Fig. 5, Row 3	5.08	1.08	0.98	2.22	926.13	16.87	240.21	11.34	**0.12**	**0.13**

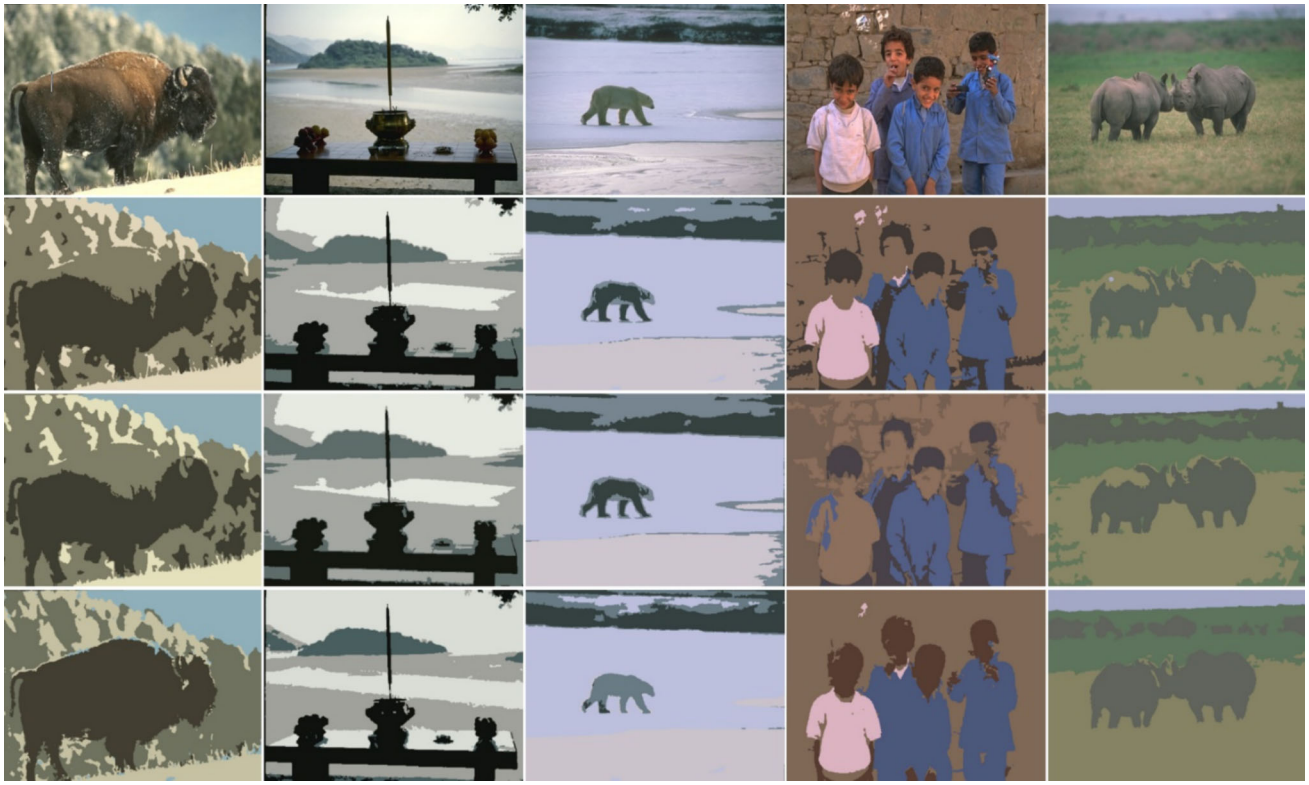

Fig. 13 Comparison of segmentation results on color images from BSDS500 (*c=4*). (Row 1) Original images. (Row 2) FRFCM results. (Row 3) RFCM results. (Row 4) IGK results

Table 10 Execution times of various algorithms on color images (seconds)

Image	Fig. 7, Row 1	Fig. 7, Row 2	Fig. 7, Row 3	Fig. 7, Row 4	Fig. 7, Row 5	Fig. 8, Row 1	Fig. 8, Row 2	Fig. 8, Row 3	Fig. 8, Row 4	Fig. 8, Row 5
RFCM	1.30	2.64	1.56	1.28	1.11	3.86	2.16	1.40	2.52	4.58
FRFCM	**0.98**	**1.57**	**0.98**	**0.90**	**0.91**	**1.44**	**1.42**	**1.13**	**1.54**	**2.16**
IGK	1.30	1.86	1.76	1.36	1.45	4.49	2.40	1.70	2.10	3.85

were followed, which included the use of various sequences such as (repetition time (TR) = 4800 ms, echo time (TE) =105 ms, flip angle (FA) = 90º, field of view (FOV) = 230 × 230 mm^2, number of slices = 20, acquisition matrix = [0, 352, 256, 0], voxel size = 0.33 × 0.33, slice thickness = 5 mm). Labelling process of used images were carried out by a radiologist with over 20 years of experience in assessing MRI scans. Here, we set *c=4* for all cases.

The images were preprocessed to remove skull and scalp areas before segmentation. Fig. 6 and Table 4 illustrate IGK's capability to preserve lesion edges and capture compact clusters within MS-affected brain areas. Comparatively, FCM, GK, and ARKFCM algorithms were less effective at distinguishing MS lesions. The Jaccard criterion highlights IGK's edge-preservation ability, surpassing other methods like EnFCM, RFCM, and FRFCM, which struggled with spatial information acquisition critical for representing compact MS clusters accurately. Overall, IGK demonstrated potential as a segmentation tool in medical image analysis, offering valuable support for specialists in diagnosing and assessing neurodegenerative diseases such as MS.

4.5 Results of Color Images

Segmenting color images with different cluster shapes challenges most FCM-based methods, largely due to difficulties in capturing spatial information. In IGK, color image segmentation clusters individual pixels rather than relying on grayscale histograms, as color image histograms are more complex to obtain. To optimize data distribution, multivariate morphological reconstruction (MMR) [45] is applied, with the remaining steps similar to grayscale segmentation. The block diagram of this method is presented in Fig. 7. The first step involves data transformation where the RGB

Table 11 Computational complexity of different fuzzy-based algorithms

Algorithms	Computational Complexity
FCM	$O(N \times C \times T)$
GK	$O(N \times C \times T)$
EnFCM	$O(T \times q \times C)$
FGFCM	$O(N \times W^2 + q \times C \times T)$
FLICM	$O(N \times C \times T \times W^2)$
ARKFCM	$O(N \times C \times T)$
KWFLICM	$O(N \times C \times T \times W)$
RFCM	$O(T \times q \times C)$
FRFCM	$O(N \times W^2 + q \times C \times T)$
IGK	$O(N \times W^2 + q \times C \times T + N \times C)$

image is projected into a decorrelated color space using Principal Component Analysis (PCA), enhancing the separation of chromatic and luminance information. To encode spatial and spectral characteristics, synthetic grayscale representations are constructed through a nonlinear transformation combining PCA components and RGB channels with carefully designed scalar weightings. Grayscale morphological reconstruction is then independently applied to each transformed representation, suppressing noise and enhancing homogeneous regions while maintaining edge integrity. The reconstructed outputs are decoded through inverse transformation, generating a refined RGB image with enhanced spatial coherence and contrast stability. MMR operation reserves color structure through PCA-based multichannel encoding and enhances robustness in low-contrast and noisy regions. For additional methodological details, refer to [45].

Previous studies [9,26] have shown that FRFCM and RFCM outperform FCM, EnFCM, FGFCM, FLICM, ARKFCM, and KWFLICM in color image segmentation. Consequently, we compare IGK with FRFCM and RFCM, using different cluster centers (c=*2*, c=*3*, and c=*4*).

Fig. 8 and Table 5 present visual and quantitative comparisons on BSDS500 images, respectively. Results indicate that IGK achieves better segmentation than FRFCM and RFCM, preserving more edges and detailed features. IGK attains the highest values in *CS*, *DS*, and *JS* criteria, while FRFCM and RFCM show similar values. This suggests that using Euclidean distance in FCM-based methods neglects distance variations within data points in similar clusters.

A second set of images from the MSRC dataset was analyzed (Fig. 9, Table 6). FRFCM and RFCM incorrectly

Table 12 Comparison of convergence and stability in different algorithms

Aspect	IGK	ARKFCM	RFCM	FRFCM	FLICM
Cost Function	Robust to noise and outliers with Mahalanobis distance	Kernelized FCM and adaptive scale tuning	FCM with robust cost functions to reduce sensitivity to outliers	Modified FCM using spatial filtering and robust cost function	FCM with local spatial regularization term
Distance Criterion	Mahalanobis	Kernel-based	Euclidean	Euclidean	Euclidean
Adaptive Distance	Yes	Yes	No	No	No
Spatial Model	MR + median filter (modular)	Adaptive kernel influence	Histogram-based with adaptive feature	Using window-based filtering	Local similarity (on pixels)
Histogram-Based	Yes	No	Yes	Yes	No
Noise Robustness	Very High	Moderate	High	Very High	Moderate
Convergence	It depends on covariance matrix; may suffer from singularity	It depends on proper kernel and tuning conditions	Monotonic convergence under appropriate optimization framework	monotonic convergence in practical settings	Monotonic convergence; slow convergence under local update
Stability	High	It depends on kernel and scale parameters	Improved stability due to reduced sensitivity to extreme values	High	Moderate; scalar local fuzzy terms used
Computational Complexity	Moderate	High; due to kernel evaluations and adaptations	Low-Moderate; avoids high-order matrix operations	Low to moderate; optimized for fast execution	High; local terms require neighbor analysis
Recommended Application Scenario	Clusters with ellipsoidal shapes or varying orientations	Nonlinear and noisy data with complex decision boundaries	Scenarios with significant noise or outliers	High-speed segmentation in noisy image settings	Edge-preserving clustering in highly corrupted data

Table 13 Advantages and disadvantages of different algorithms

Algorithm	Advantages	Disadvantages
IGK	- Adapts to different cluster shapes via an adaptive metric- Suitable for elliptical or anisotropic distributions- Better than FCM-based approaches for shaped clusters- Robust to different noises due to adaptive distance criterion- Appropriate for ellipsoidal distribution in color images- Robust to varying illumination- Strong structure preservation	- High computational complexity due to Sensitivity to covariance matrix singularity– Not spatial
ARKFCM	- Robust to noise via adaptive kernel functions- Captures nonlinear cluster boundaries- Good performance in nonlinear spaces and medical images	- Computationally heavy due to kernel calculations- Sensitive to kernel and parameter choice- Requires fine-tuning to guarantee convergence- Not suitable for anisotropic distributions- High Execution times- Require to fine-tuning for different datasets
RFCM	- Uses robust loss functions for noise resistance- No matrix regularization required- Increased stability over classic FCM	- Lacks spatial noise modeling- It depends on cost function- Not appropriate for spatially structured data- Lack a locally adaptive distance metric on color images- Accuracy decreases as the number of cluster centers increases- Not suitable to model non-linear color spaces
FRFCM	- Very fast and efficient- Effective for different noise in images- Simpler implementation	- Lower accuracy in textured or structured data- Limited shape flexibility- Not suited for nonlinear distributions- Accuracy decreases as the number of cluster centers increases- May over-smooth regions in detailed textures- Not suitable to model non-linear color spaces- Lack a locally adaptive distance metric on color images
FLICM	- Edge structure preservation	- Slower due to local term computation- Higher computational cost- Less optimal for time-constrained applications- High Execution times- Not appropriate for color images

labeled parts of an object as background in several cases, resulting in lower *CS* indices. In the fifth image, leaves are misclassified as part of the object class, indicating that distance metrics in FRFCM and RFCM may not adapt well to complex cluster shapes. These findings highlight IGK's advantage in accommodating diverse cluster shapes through elliptical modeling.

For facial reconstruction surgeries, skin segmentation is crucial in both pre- and post-surgery assessments [46]. We evaluated IGK's effectiveness in facial skin segmentation using five images from the SUT dataset. Figure. 10 and Table 7 compare IGK with FRFCM and RFCM. FRFCM and RFCM often failed in shadowed or inhomogeneous areas, misclassifying non-skin pixels as skin. In contrast, IGK demonstrated robustness to varying illumination and effectively extracted facial contours, aiding in facial landmark localization. Table 7 confirms IGK's superior performance in all criteria, especially in preserving edges, making it a valuable tool in facial surgery applications.

MRI image segmentation is a crucial tool for assisting neurosurgeons and radiologists in diagnosing various conditions. This process involves dividing an image into three distinct, non-overlapping classes: white matter (WM), gray matter (GM), and cerebrospinal fluid (CSF) [47]. Different MRI modalities are utilized to enhance clinical diagnoses by capturing specific features that reveal unique soft tissue contrasts. These modalities include T1-weighted MRI (T1), T2-weighted MRI (T2), and Fluid-Attenuated Inversion Recovery (FLAIR). T1 images highlight healthy tissues with high intensity and pathologies with low intensity, whereas T2 images depict pathologies with high intensity. FLAIR images are particularly useful for identifying edema regions by suppressing signals from water molecules. Combining these modalities is an effective approach for fusing complementary information, thereby improving diagnostic accuracy. These fused images are better suited to assist specialists in interpretation and treatment planning [48–50].

We evaluated IGK's performance in segmenting five fused MRI images from different modalities. These images were presented in the axial plane with 1 mm slice thickness, 3% noise, and 20% intensity non-uniformity, using an anatomical model with 0% noise and 0% RF as ground truth. After normalization and skull stripping, the fused modalities were segmented. Visual and quantitative comparisons between IGK and two benchmark algorithms are shown in Fig. 11 and Table 8, respectively. Experimental results for the seg-

mentation of WM, GM, and CSF using IGK, FRFCM, and RFCM are detailed in Table 8.

The high values of *CS*, *DS*, and *JS* criteria for WM tissues indicate accurate segmentation by the IGK algorithm. While three algorithms performed well in WM segmentation, RFCM performed suboptimally in GM segmentation as shown by the JS index. Since GM forms a compact cluster, FCM-based approaches using Euclidean distance struggled with mislabeling CSF and GM pixels, as seen in Fig. 11. IGK achieved the highest *CS*, *DC*, and *JS* values, highlighting its robustness to noise and resistance to intensity inhomogeneity. Both FRFCM and RFCM were less effective for CSF segmentation, with numerous misclassified CSF pixels (see Figure 10). The compact shape of the CSF region suggests that FCM-based approaches struggle when clusters have different shapes and sizes, supporting IGK's suitability for detecting ellipsoidal clusters with varying sizes and orientations.

We further illustrated IGK's performance in color image segmentation by segmenting BSDS500 images with different numbers of clusters. As seen in the first image of Fig. 12, IGK accurately separated the object from backgrounds in two-cluster segmentation, unlike FRFCM and RFCM. With more clusters, IGK continued to outperform its peers. In the third image of Fig. 12, FRFCM and RFCM incorrectly classified the basket region, while IGK successfully segmented the background, object, and basket. In another case, where the object cluster is smaller and more compact, FRFCM and RFCM failed to segment it correctly in two-cluster segmentation ($c=2$), but IGK overcame this challenge by adapting to elliptical data distributions. With three clusters ($c=3$), IGK outperformed its peers. In the fifth image of Fig. 12, FRFCM and RFCM mislabeled skin pixels due to the compact cluster shape, while IGK segmented them accurately. In the final case, IGK again demonstrated superior performance.

In color image segmentation with four clusters ($c=4$), FRFCM and RFCM lack locally adaptive distance metrics, making them less effective. IGK addresses this limitation by using Mahalanobis distance as a dissimilarity measure, offering greater robustness. This improvement is demonstrated through segmentation of five BSDS500 images with four clusters ($c=4$). For instance, as illustrated in Fig. 13, IGK accurately segments the object in the first and third images, while in the fourth image, FRFCM and RFCM misclassify facial pixels due to inadequate distance variation handling within clusters, underscoring IGK's adaptability to data point distributions.

We also compared the execution times for grayscale and color images segmentation (Tables 9 and 10). Table 9 shows that the computational cost for FLICM and KWFLICM was substantially higher in grayscale image segmentation, whereas FRFCM and IGK were considerably faster. However, in color image segmentation, IGK was not faster than its peers.

Table 11 provides a comprehensive analysis of computational complexity across fuzzy clustering algorithms. IGK demonstrates fast and stable convergence due to its histogram-based design and integration of MR operation and adaptive distance metrics, which guide the clustering process structurally. Both IGK and FRFCM utilize histogram-based clustering rather than pixel-wise updates, unlike FLICM. FLICM offers strong robustness to noise and outliers owing to its local spatial information modeling; however, it often suffers from slow convergence due to repetitive local context evaluations at each iteration. RFCM, optimized for residual modeling, demonstrates faster convergence, particularly in noisy or degraded imaging conditions. ARKFCM and FRFCM achieve moderate convergence rates by balancing spatial regularization with kernel-based enhancements. Notably, IGK offers superior convergence speed by avoiding exhaustive pixel-level iterations, making it especially effective for processing large-scale images.

4.6 Advantage and Disadvantage Comparison

Based on the related literature reviews and obtained experimental results, we conducted an extensive, comparative analysis focusing on convergence and stability to highlight the strengths and limitations of each algorithm. Table 12 compares the convergence behavior, stability properties, and mathematical regularization strategies of IGK, FLICM, ARKFCM, FRFCM, and RFCM algorithms. Table 13 summarizes the advantages and disadvantages of these algorithms.

5 Conclusion

Traditional FCM-based approaches using Euclidean distance often inadequately capture the distance variation among data points within clusters, particularly in color images or clusters with diverse shapes and sizes. Most existing methods struggle with efficient segmentation across varying cluster geometries due to limited spatial information acquisition. the proposed IGK algorithm addresses these limitations by incorporating the Mahalanobis distance metric, which better accommodates non-uniform cluster structures, and utilizing MR operator-based reconstruction to preserve object edges under noise. Unlike Euclidean distance, Mahalanobis distance captures data covariance structure, allowing clustering to adapt to anisotropic and correlated feature distributions critical for handling elliptical clusters and multivariate pixel features in medical and natural color images. MR contributes a topology-preserving spatial prior, enhancing the structural consistency, while median filter on the membership matrix

stabilizes the adaptive feature space, improving convergence in degraded conditions. Experimental results indicate that IGK performs well in segmenting both grayscale and color images without requiring parameter tuning, a significant advantage in practical applications. Future work could focus on developing an enhanced version of the GK algorithm that automatically determines the optimal number of clusters, potentially improving adaptability and applicability in diverse image segmentation tasks.

Funding: Not applicable.

Data Availability Statement: The authors declare that used data in this article are available.

Declarations

Authors Contributions: All authors contributed to the study conception and design. Material preparation, data collection and analysis were performed by [Ali Fahmi Jafargholkhanloo], [Mousa Shamsi], [Mahdi Bashiri Bawil] and [Sebelan Danishvar]. The first draft of the manuscript was written by [Ali Fahmi Jafargholkhanloo] and all authors commented on previous versions of the manuscript. All authors read and approved the final manuscript.

Ethical approval: All procedures performed in studies involving human participants were in accordance with the ethical standards of the institutional and/or national research committee and with the 1964 Helsinki declaration and its later amendments or comparable ethical standards.

Competing interests: Not applicable.

References

1. Hamza, A., et al.: Csfcm: an improved fuzzy c-means image segmentation algorithm using a cooperative approach. Expert Syst. Appl. **166**, 114063 (2021)
2. Sensen, S., et al.: Image segmentation based on fuzzy low-rank structural clustering. IEEE Trans. Fuzzy Syst. **31**(7), 2153–2166 (2023)
3. Essam, H., et al.: An efficient multilevel thresholding segmentation method for thermography breast cancer imaging based on improved chimp optimization algorithm. Expert Syst. Appl. **185**, 115651 (2021)
4. Guoyuan, M., Yue, X.: An improved whale optimization algorithm based on multilevel threshold image segmentation using the otsu method. Eng. Appl. Artif. Intell. **113**, 104960 (2022)
5. Bin, D., et al.: An active contour model based on shadow image and reflection edge for image segmentation. Expert Syst. Appl. **238**, 122330 (2024)
6. Yiyang, C., et al.: An active contour model for image segmentation using morphology and nonlinear poisson's equation. Optik **287**, 170997 (2023)
7. El-Taraboulsi, J., et al.: Deep neural network architectures for cardiac image segmentation. Artif. Intel. Life Sci. **4**, 100083 (2023)
8. Tahereh, H., et al.: EEvoU-Net: an ensemble of evolutionary deep fully convolutional neural networks for medical image segmentation. Appl. Soft Comput. **143**, 110405 (2023)
9. Tao, L., et al.: Significantly fast and robust fuzzy c-means clustering algorithm based on morphological reconstruction and membership filtering. IEEE Trans. Fuzzy Syst. **26**(5), 3027–3041 (2018)
10. Tao, L., et al.: Superpixel-based fast fuzzy c-means clustering for color image segmentation. IEEE Trans. Fuzzy Syst. **27**(9), 1753–1766 (2018)
11. László, S., et al.: MR brain image segmentation using an enhanced fuzzy c-means algorithm. Proc. 25th Annual Int. Conf. IEEE Eng. Med. Biol. Soc. **1**, 724–726 (2003)
12. Weiling, C., Zhang, D.: Fast and robust fuzzy c-means clustering algorithms incorporating local information for image segmentation. Pattern Recogn. **40**(3), 825–838 (2007)
13. Stelios, K., Chatzis, V.: A robust fuzzy local information c-means clustering algorithm. IEEE Trans. Image Process. **19**(5), 1328–1337 (2010)
14. Maoguo, G., et al.: Fuzzy c-means clustering with local information and kernel metric for image segmentation. IEEE Trans. Image Process. **22**(2), 573–584 (2012)
15. Ivana, D., Philips, W.: Spatially coherent fuzzy clustering for accurate and noise-robust image segmentation. IEEE Signal Process. Lett. **20**(4), 295–298 (2013)
16. Deliang, X., et al.: A kernel clustering algorithm with fuzzy factor: application to SAR image segmentation. IEEE Geosci. Remote Sens. Lett. **11**(7), 1290–1294 (2013)
17. Ahmed, E., et al.: Segmentation of brain tissues from magnetic resonance images using adaptively regularized kernel-based fuzzy c-means clustering. Comput. Math. Methods Med. **2015**, 485495 (2015)
18. Mohamad Amin, B.: Segmentation and enhancement of brain MR images using fuzzy clustering based on information theory. Soft Computing **21**, 6633–6640 (2017)
19. Jian, Y., Yang, M.S.: Deterministic annealing gustafson-kessel fuzzy clustering algorithm. Inf. Sci. **417**, 435–453 (2017)
20. Xiangzhi, B., et al.: Intuitionistic center-free FCM clustering for MR brain image segmentation. IEEE J. Biomed. Health Inform. **23**(5), 2039–2051 (2018)
21. Xiangzhi, B., et al.: Similarity measure-based possibilistic FCM with label information for brain MRI segmentation. IEEE Trans. Cybern. **49**(7), 2618–2630 (2018)
22. Fankui, H., Wang, X.: An intuitionistic kernel-based fuzzy c-means clustering algorithm with local information for power equipment image segmentation. IEEE Access **8**, 4500–4514 (2020)
23. Dhirendra, K., Kumar, P.: Bias-corrected intuitionistic fuzzy c-means with spatial neighborhood information approach for human brain MRI image segmentation. IEEE Trans. Fuzzy Syst. **30**(3), 687–700 (2020)
24. Xiaolei, Z., et al.: Robust image segmentation using fuzzy c-means clustering with spatial information based on total generalized variation. IEEE Access **8**, 95681–95697 (2020)
25. Cong, W., et al.: Sparse regularization-based fuzzy c-means clustering incorporating morphological grayscale reconstruction and wavelet frames. IEEE Trans. Fuzzy Syst. **29**(7), 1826–1840 (2020)

26. Cong, W., et al.: Residual-driven fuzzy c-means clustering for image segmentation. IEEE/CAA J. Autom. Sinica **8**(4), 876–889 (2020)
27. Maria, M.A., Campilho, A.: Segmentation of retinal blood vessels by combining the detection of centerlines and morphological reconstruction. IEEE Trans. Med. Imaging **25**(9), 1200–1213 (2006)
28. Jiann-Jone, C., et al.: Object segmentation of database images by dual multiscale morphological reconstructions and retrieval applications. IEEE Trans. Image Process. **21**(2), 828–843 (2011)
29. Bezdek, J.C., et al.: FCM: the fuzzy c-means clustering algorithm. Comput. Geosci. **10**(2–3), 191–203 (1984)
30. Raghu, K., Kim, J.: A note on the gustafson-kessel and adaptive fuzzy clustering algorithms. IEEE Trans. Fuzzy Syst. **7**(4), 453–461 (1999)
31. Dejan, D., Škrjanc, I.: Recursive clustering based on a gustafson-kessel algorithm. Evol. Syst. **2**(1), 15–24 (2011)
32. Babuka, R. Van., Veen, P.J., Kaymak, U.: Improved covariance estimation for gustafson-kessel clustering. IEEE Int Conf Fuzzy Syst **2**, 1081–1085 (2002)
33. Donald, G., Kessel, W.C.: Fuzzy clustering with a fuzzy covariance matrix, IEEE conference on decision and control including the 17th symposium on adaptive processes, (1979)
34. Tao, L., et al.: Adaptive morphological reconstruction for seeded image segmentation. IEEE Trans. Image Process. **28**(11), 5510–5523 (2019)
35. Luc, V.: Morphological grayscale reconstruction in image analysis: applications and efficient algorithms. IEEE Trans. Image Process. **2**(2), 176–201 (1993)
36. Ahmed, M.N., et al.: A modified fuzzy c-means algorithm for bias field estimation and segmentation of mri data. IEEE Trans. Med. Imag **21**(3), 193–199 (2002)
37. Ali Fahmi, J., Shamsi, M.: Quantitative analysis of facial soft tissue using weighted cascade regression model applicable for facial plastic surgery. Signal Proc. Image Commun. **121**, 117086 (2024)
38. Arbeláez, P., et al.: Contour detection and hierarchical image segmentation. IEEE Trans. Pattern Anal. Mach. Intell. **33**(5), 898–916 (2011)
39. http://research.microsoft.com/downloads
40. Bakhshali, M., et al.: Evaluation of facial soft tissue parameters for Northwestern students in Iran. J. Craniomaxillofac. Res, 78–82 (2015)
41. https://brainweb.bic.mni.mcgill.ca/cgi/brainweb1
42. Orcan, A., Dolezal, R.: Distribution-based imaging for multiple sclerosis lesion segmentation using specialized fuzzy 2-means powered by nakagami transmutations. Appl. Soft Comput. **108**, 107481 (2021)
43. Jingjing, W., et al.: An adaptive sparse bayesian model combined with probabilistic label fusion for multiple sclerosis lesion segmentation in brain MRI. Futur. Gener. Comput. Syst. **105**, 695–704 (2020)
44. Zahra, M., et al.: CycleFormer: Brain tissue segmentation in the presence of Multiple Sclerosis lesions and Intensity Non-Uniformity artifact. Biomed. Signal Process. Control **93**, 106153 (2024)
45. Tao, L., et al.: A conditionally invariant mathematical morphological framework for color images. Inf. Sci. **387**, 34–52 (2017)
46. Ali Fahmi, J., et al.: Angular photogrammetric analysis of facial soft tissue by image processing algorithms. Aesthetic Plastic Surgery **48**(7), 1426–1435 (2024)
47. Chandan, S., Bala, A.: An unsupervised orthogonal rotation invariant moment based fuzzy c-means approach for the segmentation of brain magnetic resonance images. Expert Syst. Appl. **164**, 113989 (2021)
48. Jun, L., et al.: Multi-modality MRI fusion with patch complementary pre-training for internet of medical things-based smart healthcare. Information Fusion **107**, 102342 (2024)
49. Nachwa, A., Crowley, J.L.: Color-based fusion of mri modalities for brain tumor segmentation,International Conference on Medical Imaging and Computer-Aided Diagnosis, (2022)
50. Yin, F., Zongxi, S.: Medical image fusion based on feature extraction and sparse representation. Int. J. Biomed. Imaging **2017**, 3020461 (2017)

Ali Fahmi Jafargholkhanloo was born in Ardabil, Iran, in 1992. He received his B.Sc. degree in Biomedical Engineering (major: Bio-Electric) from Islamic Azad University. In 2015 he joined the Sahand University of Technology, Tabriz, Iran. He received his M.Sc. degree in Biomedical Engineering (major: Bio-Electric) from this university in 2017. He received his PhD. degree in Biomedical Engineering (major: Bio-Electric) from Sahand University of Technology, in May 2023. He is currently an assistant professor at University of Mohaghegh Ardabili. Interest include Biomedical Image Processing, Machine Learning, Meta-Heuristic Algorithms, Pattern Recognition and Facial Beauty Analysis.

Mousa Shamsi was born in Tabriz, Iran, in 1972. He graduated from high school (major: Mathematics-Physics) in Tabriz, in 1990. He passed the university entrance examination for engineering studies in Iran with a rank of 230 (out of 500,000 participants) in 1990, and joined Tabriz University. He received his B.Sc. degree in Electrical Engineering (major: electronic) from Tabriz University, in 1995. In 1996, he joined the University of Tehran, Tehran, IRAN. He received his M.Sc. degree in Electrical Engineering (major: Biomedical Engineering) from this university in 1999. From 1999 to 2002, he taught as a lecturer at the Sahand University of Technology, Tabriz, Iran. In 2002, he passed the doctoral course entrance examinations [in the field of Electrical Engineering], held by Ministry of Culture and Higher Education [MCHE] of Iran, and entered the University of Tehran as a PhD Candidate. From 2002 to 2008, he was a PhD student at the University of Tehran in Bioelectrical Engineering. In 2006, he was granted with the Iranian government scholarship as a visiting researcher at the Ryukyus University, Okinawa, Japan. From December 2006 to May 2008, he was a visiting researcher at this University. He received his PhD degree in Electrical Engineering (major: Biomedical Engineering) from University of Tehran in December 2008. From December 2008 to April 2013, he was an assistant professor at Faculty of Electrical Engineering, Sahand University of Technology, Tabriz, Iran. From April 2013 to June 2019, he was an associate professor at Faculty of Biomedical Engineering, Sahand University of Technology, Tabriz, Iran. From July 2019, he is a professor at this University.

Mahda Bashiri Bawil holds an M.Sc. in Biomedical Engineering from the University of Tehran and a Ph.D. in Biomedical Engineering from Sahand University of Technology. His research interests lie at the intersection of artificial intelligence, machine learning, medical image processing, and neuroscience. His recent work focuses primarily on brain MRI analysis for the study and early detection of neurodegenerative diseases such as multiple sclerosis (MS). He has published several scientific papers on brain tissue segmentation, automated disease progression analysis, and preoperative simulation in craniofacial surgeries. His research aims to advance the integration of engineering methods into clinical practice for improved diagnosis and treatment planning.

Sebelan Danishvar received a PhD in Electrical and Computer Engineering in 2007. He is currently a Research Fellow in the Systems Engineering Research Group (SERG) at the College of Engineering, Design and Physical Sciences, Brunel University London. His expertise includes Artificial Intelligence and Machine Learning (specializing in Deep Learning, Human-Centered AI, Reinforcement Learning, and foundational principles of ML), Data Analytics, and Signal and Image Processing and Analysis (including Image Fusion and Registration). Additionally, he is skilled in developing Computer Vision and Machine Vision applications with algorithms for image recognition and spectral analysis, particularly in industrial and medical domains. Dr. Sebelan Danishvar possesses extensive programming experience in Python, MATLAB, and C++. He has contributed to high-profile projects such as HISTEED, ZFactor, ZBreak, AFWERX, and CALM and at SERG and is currently involved in projects BIORECER and DIGINTRACE. His research aligns with promoting sustainable energy technologies, leveraging innovative AI and ML models to address complex industrial challenges.